FINAL REPORT

on
Grant NAGW-920

1 August 1986 through 28 February 1990

Use of Microwave Satellite Data to Study Variations in Rainfall Over the Indian Ocean

Principal Investigator David W. Martin

Co-Investigator Barry B. Hinton

Prepared by
Barry B. Hinton
David W. Martin
Brian Auvine
and
William S. Olson

Space Science and Engineering Center
1225 West Dayton Street
University of Wisconsin-Madison
Madison, Wisconsin 53706

for

National Aeronautics and Space Administration
Washington, D.C.

March 1990

TABLE OF CONTENTS

1.0 INTRODUCTION

1.1 Study Objective and Approach

The University of Wisconsin Space Science and Engineering Center has mapped rainfall over the Indian Ocean using a newly developed Scanning Multichannel Microwave Radiometer (SMMR) rain-retrieval algorithm. Our short-range objective has been to characterize the distribution and variability of Indian Ocean rainfall on seasonal and annual scales. In the long-range, our objective is to clarify differences between land and marine regimes of monsoon rain.

To accomplish these ends we have developed a semi-empirical algorithm for retrieving Indian Ocean rainfall. Tools for this development have come from radiative transfer and cloud liquid water models. Where possible, ground truth information from available radars (U.S. Gulf Coast) has been used in development and testing. SMMR rainfalls have also been compared to Indian Ocean island gauge rainfalls. Final Indian Ocean rain maps have been produced for months, seasons, and years and interpreted in terms of historical analyses of rain over the sub-continent.

1.2 Uniqueness of SMMR

SMMR has provided global observations of microwave radiation for nearly a decade, beginning in late 1978. This length of record offers a unique opportunity for a climatological view of rainfall. Because SMMR has been operational long enough to have been the focus of prior investigations, technical subjects ranging from data access and processing to sensor character and response have been well documented and are readily available. Rainfall retrieval methods which have found their way into the literature have been helpful in finding an algorithm that would meet the needs of this regional climatological study.

1.3 Need for a New Algorithm

The main criteria for the design of a rain rate retrieval algorithm in this study are (1) that it yield estimates of the average rainfall rate over $1^{o} \times 1^{o}$ areas, (2) that it exploit the spectral information in the SMMR channels, (3) that it yield accurate rain estimates over the Indian Ocean, in particular, and (4) that it be computationally efficient, so that the hundreds of overpasses comprising the three year study period could be processed at a reasonable cost. The SMMR rain rate retrieval algorithm developed by Prabhakara, *et al.* (1986) comes close to meeting these criteria. The Prabhakara, *et al.* algorithm yields estimates of the cloud liquid water content using the 6.6 and 10.7 GHz channels of SMMR, from which the precipitation rate is inferred using empirical relationships. However, we believe that by taking a more model-based approach to the rain retrieval problem, and by combining the model relationships with a statistical description of tropical rainfall distributions, we can obtain an improved algorithm which in addition satisfies criteria (2) and (3) above.

2.0 DATA

The data required for this research were the brightness temperatures from the ten channels of the SMMR. This instrument has been described by Gloersen and Hardis (1978). SMMR data from about three years (December 1978 thru December 1981) were made available from the National Space Science Data Center (NSSDC) on TCT tapes, courtesy of Per Gloersen.

For comparison of SMMR radiances and radar rain rates, data from two National Weather Service WSR-57 radars were available in digitized format for hurricanes approaching the coast on September 3, 1979 at Miami (David) and August 17, 1983 Galveston (Alicia), respectively. While not ideal for the purpose of calibrating our algorithm to the Indian Ocean, these cases did provide a relatively broad range of rain rates. NOAA Hurricane Research Division personnel (Frank Marks and Peter Dodge), who supplied the data, also suggested a Z-R relationship with which to compute rain rates. We attempted to use a Daytona Beach radar data set, provided by Raul Lopez, for a summer period during 1983. However, the scanty coverage and low rain rates when compared to SMMR at satellite resolution, resulted in relatively little useful information.

For a description of the Indian gauge data used in the validation of our final results, see Section 4.2.1.

3.0 ALGORITHM DEVELOPMENT

3.1 Approach

In our study we primarily adopted a modelling approach. The alternative of empirically determining the relationship between rain rate and the brightness temperatures was precluded by a scarcity of observational data.

Specifically, the goal of the modelling was to determine, for each channel, the distribution of possible upwelling microwave brightness temperatures which could be measured by the SMMR for a given average rainfall rate within a 1° by 1° square area. In order to accomplish this both a physical model, which describes the transfer of microwave radiances through precipitating clouds, and a statistical model, which describes the spatial distributions of rain within a 1° square, are required. The development of the radiative transfer model is reviewed in section 3.1.1. In section 3.1.2 input data consistent with environmental conditions over the Indian Ocean are specified, and the resulting computed upwelling brightness temperatures are presented in section 3.1.3. The model brightness temperatures in each of the SMMR channels are averaged over realistic rainfall rate distributions in section 3.1.4.

3.1.1 Radiative transfer cloud model

It is customary to express microwave radiances in a wavelength or frequency band at microwave frequencies in terms of the equivalent brightness temperature T_B -- the temperature an ideal black body would have if it were emitting the same radiance. (Each material has an emissivity ϵ, such that $T_B = \epsilon T$ if T is the thermometric temperature; a black body has unit emissivity.)

Basic processes determining the microwave radiance upwelling from the earth-atmosphere system are emission, absorption, and scattering. A radiometer looking along a narrow beam will see radiation emitted in that direction from the surface, less any absorbed or scattered from the beam by the intervening atmosphere, clouds, or precipitation.

Added to the radiation it sees will be a contribution from radiation emitted by the earth in other directions, but subsequently scattered into the beam. There are also contributions from the radiation emitted into the beam by every layer of the atmosphere and by the cloud and precipitation particles immersed in the atmosphere. Some of this radiation too, is subsequently scattered out of the beam or absorbed. These processes are described by the equation of radiative transfer.

Using the dielectric and conductivity properties of water, one can derive Fresnel's reflection formulas. The emission coefficient for water follows from Kirchoff's law. Emissivity and reflectivity vary with the polarization and direction relative to the surface. Since electromagnetic properties of water vary with temperature and with salinity, so do the emissivity and reflectivity, fresh water having somewhat different properties than sea water. Due to resonance-relaxation effects of water, emissivity and reflectivity depend upon the frequency and polarization of the electromagnetic wave. For the 50° incidence angle of SMMR the emissivity of sea water is the order of 0.4. The surface temperature is about 300 K, so the surface emission will be the order of 120 K. The effective emissivity increases with the wind, due to the roughening and consequent distribution of slopes which produces a distribution of incidence angles, and due to the structure of the foam produced by the wind.

Clear-air atmospheric absorption and emission effects are almost entirely due to the spectral absorption lines of gas phase H_2O and O_2, and must therefore be calculated based on altitude profiles of temperature, pressure, and some measure of moisture, such as relative or specific humidity. Extinction coefficients, k_{ext}, are highest at 100% relative humidity. For SMMR frequencies these are < 0.06 (in units of km^{-1}), except for 21 GHz, which is near the center of the water absorption and has a value of about 0.09. The SMMR frequencies, except for the 21 GHz channels, were chosen to be in window regions of dry-atmospheric gases. Consequently, small variations in the vertical temperature and

pressure structure are of minor significance, enabling one to use standard, or fixed, profiles.

The effects of suspended liquid drops can be greater at the higher SMMR frequencies. The small diameter ($d < 0.1$ mm), non-precipitating particles making up the clouds are Rayleigh particles at SMMR frequencies, but scattering is negligible in comparison with absorption and emission. Even absorption is slight for the lowest SMMR channels (k_{abs} is the order of 0.004 km^{-1} at 6.6 GHz for "cloud" (Battan, 1973)), but ranges up to moderately large values at the highest frequency (k_{abs} is on the order of 0.15 km^{-1} at 37 GHz.) Because the temperature of the absorbing clouds at these frequencies is significantly greater than the ocean emission temperature, the 37 GHz channels, and to a lesser extent the 18 GHz channels, "see" clouds as an increase in brightness temperature.

Larger drops ($d > 0.1$ mm) precipitate. Generally, these drops are sized similarly to the Marshall-Palmer distribution, so that the idealized distribution and rain rate are uniquely linked. Precipitation particles are in the Mie-range for SMMR channels, though at the low-frequency end of this range at 6.6 and 10.7 GHz. Thus, for this group of particles, one can calculate extinction and scattering coefficients as a function of the rain rate using Mie theory, if they are assumed spherical or nearly spherical. The radiative properties of aspherical hydrometeors, which have been deformed due to aerodynamic forces, have been computed by Wu and Weinman (1984). A calculation of the hydrometeor radiative properties must be done for each layer of the atmosphere if the profile of precipitation varies or if the temperature varies.

Most rain systems in the Indian Ocean will extend above the freezing level, which is usually around 4-5 km altitude. As a consequence there will be frozen cloud particles ($d <$ 0.1 mm) suspended in the upper levels of clouds, but frozen precipitation ($d > 0.1$ mm) will also be present much of the time. For reasonable particle densities, the extinction coefficient due to frozen cloud particles is less than about 0.0005 km^{-1} at the SMMR frequencies. In the case of frozen precipitation, the extinction above 18 GHz frequency is

primarily due to scattering rather than absorption. Even though (for similar size distributions and water contents) the extinction due to frozen precipitation is much less than that due to liquid, ice will often have a pronounced effect on the upwelling brightness temperature at frequencies exceeding 18 GHz, since the ice layer can be a few kilometers thick.

Although the radiative transfer solutions for more complicated cloud vertical profiles have appeared in the literature (Weinman and Davies, 1978; Kummerow and Weinman, 1988; Olson, 1989), the radiative computations in this study are performed using a plane-parallel (horizontally-uniform) model with a vertically-stratified atmosphere. For two reasons the added complexity of finite cloud geometries is not warranted. Firstly, the statistical properties of three-dimensional rain fields, including vertical-horizontal correlations, are not well-established. In addition, the model is applied to "subgrid" areas which are very small compared to 1^{o} by 1^{o} squares. Over these small areas the rainfall rate and other atmospheric conditions are more nearly uniform, in compliance with the modelling assumption.

The plane-parallel model atmosphere is divided into 120 layers between the surface and 12 km altitude. At each layer interface the bulk extinction coefficient, albedo for single scattering, and asymmetry factor are specified. The atmospheric temperature in the model atmosphere is linearly decreasing with height, at a lapse rate of 5.41 $C \cdot km^{-1}$. The water vapor density profile is exponentially decreasing with a scale height of 2.04 km. The temperature lapse rate and water vapor scale height were derived from the annual-mean tropical data of Jordan (1958). Surface values of temperature and water vapor are prescribed in the model tests which follow in the next section.

Atmospheric oxygen and water vapor extinction coefficients are computed using the Rosenkranz (1975) and Staelin (1966) models, respectively. The extinction by non-precipitating cloud is evaluated from the Rayleigh theory. Radiative properties of precipitation-sized hydrometeors are determined from the parameterizations in Wu and

Weinman (1984). The vertical profile and phase of hydrometeors in the model are defined as in Olson (1989). Liquid cloud droplets and precipitation are uniformly distributed in the vertical between the surface and a prescribed phase transition level, while frozen precipitation and cloud particles are uniformly distributed between the phase transition level and the cloud top. The cloud top was set to 10 km in the model simulations. Although actual cloud tops are sometimes higher in the tropics, it was determined by Olson (1989) that modeled ice layers with uniform water contents between the phase transition level and 10 km yielded radiances in agreement with SMMR-measured radiances. Therefore, a similar parameterization was adopted for the present study.

The ratio of the column-integrated ice-phase particles and column-integrated liquid drops is prescribed in the radiative model. A ratio of 0.35 was derived by Olson (1989) from several radar profiles within hurricanes. This ratio also yielded model-computed radiances consistent with SMMR-measured radiances in hurricanes.

The surface boundary is characterized by the sea surface temperature, emissivity and reflectivity. The Wilheit (1979) model is used to compute the sea surface emissivity and reflectivity as functions of the surface temperature, salinity and 20-meter wind speed. (The wind speed is referred to 10 meter height in the following subsection.) The incoming radiance from space at the upper boundary is set equal to the nominal cosmic background radiance (2.7 K).

The multiple-scattering solution for the transfer of microwaves through the model atmosphere is computed using Eddington's second approximation. In our application the first-order Eddington solution is obtained for each atmospheric layer for which the radiative properties are assumed to be the average of the properties specified at the bounding layer interfaces. The undetermined coefficients in the Eddington solution are found by imposing flux continuity at the layer interfaces. The first-order Eddington solution is used to describe only the vertical/angular distribution of scattered radiation within the atmosphere. The first-order solution is used to evaluate the scattering source term in the

radiative transfer equation which is re-solved. The upwelling brightness temperature at the top of the atmosphere resulting from the second-order computation has been shown (Weinman and Davies, 1978) to agree well with precise Monte-Carlo simulations of the upwelling brightness.

Model computations of the upwelling microwave brightness temperature were found to agree within the precision of the published brightness temperature values of Weinman and Davies (1978) for simple plane-parallel cloud geometries. Model brightness temperatures generated from more complicated cloud geometries were compared to the results of Kummerow (personnel comm.), who had concurrently but independently developed a similar plane-parallel model. Over a wide range of microwave frequencies and precipitation rates, the models agreed within about 1 K. Discrepancies are attributed to a different methods for specifying the layer-average atmospheric radiative properties.

3.1.2 Radiative model "cloud-free" simulations

Next we defined base state environmental conditions in the model. The base state was chosen to approximate mean conditions over the Indian Ocean well enough that the modelled effects of variations in environmental parameters about the base state would be similar to actual effects of real variations about the mean environmental state.

We selected the mean climatological values of sea surface temperature, surface layer salinity, surface air temperature, surface relative humidity, and 10-meter wind speed as shown in Table 3.1 to define the basic cloud-free state of the model. Characteristic high and low values of sea surface temperature, surface relative humidity and 10-meter wind speed were also established, based upon the observed ranges of these parameters. (For convenience we refer to these as maximum and minimum values, but they need not be in an absolute sense.)

The radiative transfer model was first run using the base state environmental conditions (80% relative humidity), and then using the base state conditions except for the

surface relative humidity, which was assigned the extreme values of 50% and 90%. The resulting computed brightness temperatures at the SMMR frequencies are listed in the left-hand columns of Table 3.2.

TABLE 3.1. Parameters of the problem.

Variable Name	Basal Value	Units	Minimum	Maximum
Sea surface temperature	300.15	K	298.15	303.15
Surface layer salinity	34.5	o/oo	(const.)	(const.)
Surface air temperature	297.85	K	(const.)	(const.)
Surface relative humidity	80	%	50	90
Surface wind speed	7	$m \cdot s^{-1}$	2	20
Ice-liquid transition level	5	km	4	5
Columnar ice/liquid ratio	0.35	...	0	0.35
Non-precipitating cloud water content	0.2	$g \cdot m^{-3}$	0	0.6
Top of ice layer	10	km	(const.)	(const.)

The model-computed brightness temperature values were compared to actual SMMR observations over the Indian Ocean. Samples of non-raining SMMR data from several regions of the Indian Ocean at two periods, one before and one after the onset of the southwest monsoon in 1979, were examined. The samples were obtained only from nominally cloudless regions as determined from data of the Indian Ocean Geostationary Operational Environmental Satellite.

In the right-hand columns of Table 3.2 we present the means and extremes of the Indian Ocean brightness temperature samples. Pre-onset values of the SMMR-observed brightness temperatures correspond to a range of 50-85% for surface relative humidity, while post-onset values spanned brightnesses similar to those expected for 70-95% under totally cloudless skies. Recall that the modelled radiances corresponded to an expected range of 50 to 90% relative humidity. Despite the slight difference between the maximum observed and model surface relative humidities, reasonable agreement between the "cloud-

free" observed and modelled radiances is indicated by the Table 3.1. The stage was set for modelling the brightness temperatures upwelling from precipitating clouds.

TABLE 3.2 Modelled and observed microwave brightness temperatures for the Indian Ocean. Observations are averages over 8 pixel by 8 pixel (about 32 km by 32 km) GOES data boxes for three locations (each) on days 136 and 170 of 1979.

Chan.	Model			Observations		
	Mean	Max.	Min.	Mean	Max.	Min.
6.6V	159.2	159.4	158.8	161.0	163.5	159.7
6.6H	86.9	87.1	86.3	86.6	90.5	84.2
10.7V	164.6	165.0	163.5	168.1	168.8	167.1
10.7H	92.6	93.2	90.8	96.9	100.0	94.8
18V	184.6	186.5	178.5	185.6	187.6	181.6
18H	120.8	123.9	111.1	120.0	124.8	111.0
21V	218.4	222.6	203.5	214.9	223.8	203.6
21H	173.8	180.7	149.8	171.7	182.4	148.3
37V	213.4	215.8	205.7	213.5	216.6	208.9
37H	159.4	163.5	146.5	151.4	158.8	138.9

3.1.3 Radiative model simulations of precipitating clouds

Our goals were to determine the relationship between the upwelling brightness temperature and surface rainfall rate at each SMMR frequency and polarization and to quantify the impact of environmental parameters other than rain rate on that relationship. In addition to variations in the "cloud-free" environmental parameters discussed above, variations in cloud parameters, such as the water phase transition level, ice/liquid hydrometeor columnar ratio, and non-precipitating water content, were also considered in this modelling study. Base state and expected extreme values for these parameters are also listed in Table 3.1. The base value and range of each of the environmental parameters were chosen to reflect expected conditions in the Indian Ocean region. These conditions and their ranges are not much different than would apply to tropical oceans generally, but define a much more restricted problem than the "global" domain.

The first step was to calculate the upwelling brightness temperatures at the SMMR frequencies and viewing incidence angle (50°) for a range of rain rates from 0 to 64 mm•h^{-1} using the model, with environmental parameters other than the rain rate set to their base values. Figure 3.1 shows the TB(R) curves from the base state model. Since spatial resolution at 6.6 GHz is ~ 150 km and emission at 21 GHz channels is significantly affected by vapor, only 10.7, 18 and 37 GHz channels are presented. They reflect the behavior expected from many previous radiative transfer simulations. The curves are double valued in TB and peak at progressively lower rain rates as the frequency increases.

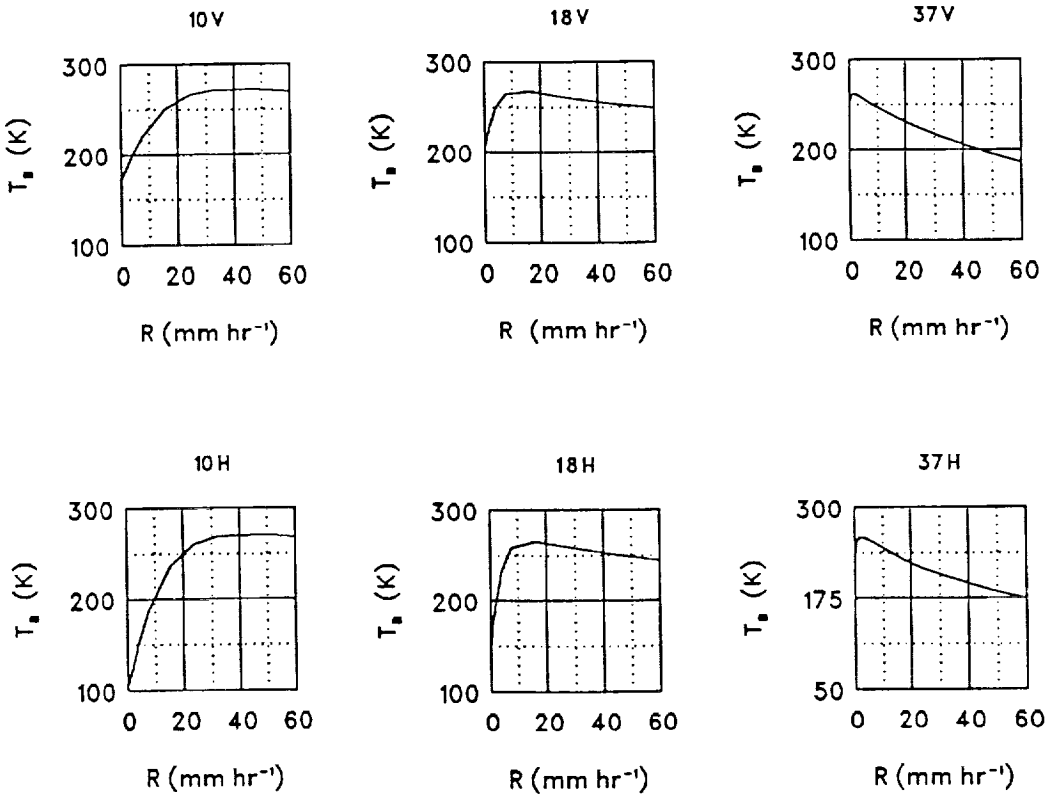

FIG. 3.1 Base state model curves for microwave brightness temperature as a function of rain rate for the 10.7, 18, and 37 GHz SMMR channels. Frequency increases left to right. Vertical polarization at the top, horizontal is at the bottom.

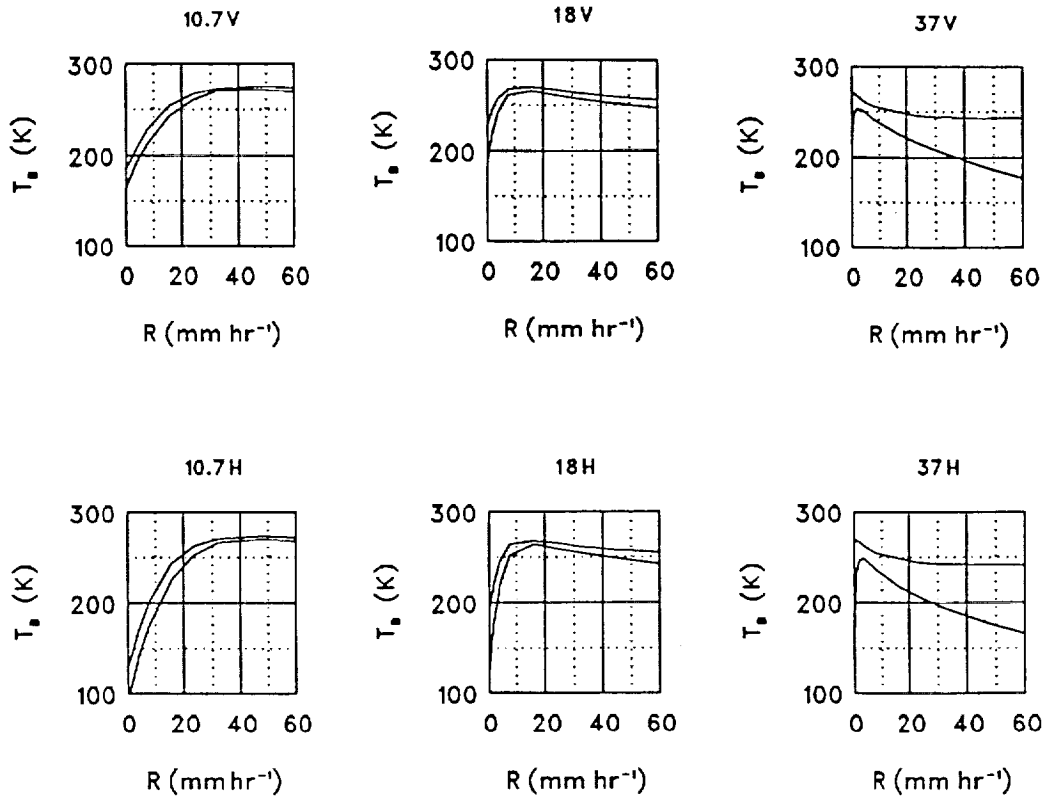

FIG. 3.2 Envelopes of the base state model curves for microwave brightness temperature as a function of rain rate for the 10.7, 18, and 37 GHz SMMR channels. Frequency increases left to right. Vertical polarization at the top, horizontal is at the bottom.

We then studied the effects of variations in the environmental parameters other than the rainfall rate. For each environmental parameter to be tested, the radiative model was run twice. In the first run all environmental parameters were set to their base state values except the test parameter, which was assigned its minimum value. In the second run the test environmental parameter was assigned its maximum value. In both runs the upwelling brightness temperature was computed for rainfall rates between 0 and 64 $mm \cdot h^{-1}$. Such runs were carried out for each secondary parameter which had a significant range of natural variation and a significant impact on the upwelling brightness temperature (see Table 3.1).

To summarize the results as briefly as possible, we show in Figure 3.2 the spread in TB values induced by all environmental parameter variations. The figure gives an indication of the error these variations would be expected to produce in a rainfall estimate from a single-channel measurement.

Investigation of the various sources of the brightness temperature spread revealed that the expected variations in non-precipitating cloud liquid water are, in general, the most potent source of brightness temperature variation. The effects of variations in the other environmental parameters are small enough to be subsumed into the brightness temperature variation due to differences in the non-precipitating water content. Figure 3.3 illustrates the spread in the 10.7 GHz V-polarized brightness temperature-rain rate relationship resulting from variations in all modelled environmental parameters and that due to a 1 $gm \cdot m^{-3}$ variation in non-precipitating cloud liquid water content.

Since the presence of non-precipitating cloud water would lead to a relatively large uncertainty in the rain rate inferred from a given single-channel SMMR measurement, and since the amount non-precipitating cloud water is often linked to the dynamical processes which also produce precipitation, we sought a semi-empirical relationship between the rainfall rate and non-precipitating liquid water content which would help remove some of the ambiguity in the brightness temperature-rain rate relationship.

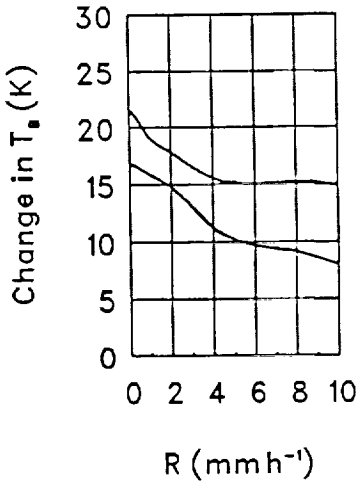

FIG. 3.3. Spread in brightness temperature as a function of rain rate for 10.7 V due to modelled variations in surface wind, temperature, cloud liquid water and humidity (upper curve) compared to the spread for a 1 $gm \cdot m^{-3}$ variation in non-precipitating cloud liquid water content alone (lower curve).

We first examined radar data from hurricanes Alicia and David, finding that agreement between model-simulated brightness temperatures based upon area-averaged radar rain rates and brightness temperatures measured by the SMMR seemed to require somewhat greater amounts of non-precipitating liquid than our base state conditions. A non-precipitating liquid water content that increased rather rapidly with rain rate initially, then at a slower rate above a few $mm \cdot h^{-1}$ seemed necessary. This trend is illustrated for the vertically polarized 10.7 GHz channel in Figure 3.4.

A similar relationship between precipitating and non-precipitating cloud water was derived from the recent one-dimensional cloud model simulations of Ridout (personal comm.). Ridout's cloud model was run for tropical ocean environmental conditions and three different prescribed updraft radii. Vertical profiles of water substance were sampled at 5 minute intervals over the lifetime of the simulated cloud in each model run. Using these profiles we fit a physically reasonable curve (3.1) relating the non-precipitating cloud liquid content, q_{cloud}, to the rainfall rate, R.

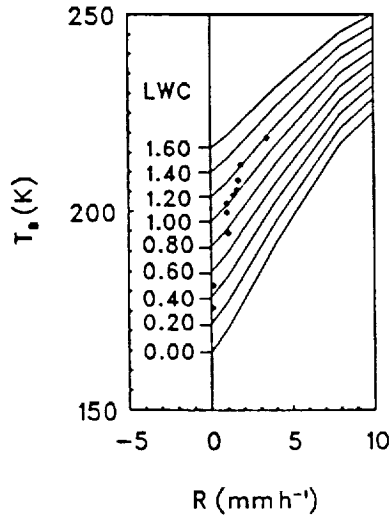

FIG. 3.4. Brightness temperature as a function of rain rate and non-precipitating water content, showing the water content required to fit the hurricane data (dots). LWC is the non-precipitating liquid water content in $g \cdot m^{-3}$.

$$q_{cloud} = 0.057 + 0.069 \cdot \ln(R+1). \qquad (3.1)$$

In single-channel retrieval studies (see section 3.2) it was determined that monthly rain accumulations were most sensitive to the magnitude of the non-precipitating liquid water content at zero rainfall rate (the first constant on the right-hand side of (3.1)). Usage of (3.1) to produce a single-channel retrieval algorithm yielded unacceptably large

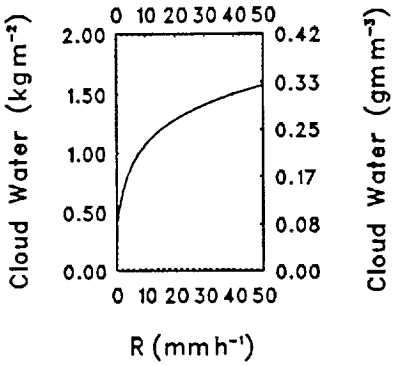

FIG. 3.5. Adopted relation between non-precipitating cloud liquid water content and rain rate.

rain accumulations for June 1979 in the Indian Ocean. In an independent study of hurricane rain retrievals using SMMR data, Olson (1989) determined that a liquid water content threshold of $0.4 gmm^{-3}$ yielded physical retrievals most consistent with coincident surface radar observations. In a model-based retrieval of cloud water distributions using Doppler radar, Hane *et al.* (1982, Figs. 13.7-13.9) shows that 0.5 $gm \cdot kg^{-1}$ of cloud water (equivalent to greater than 0.33 gm m^{-3} below 6 km altitude) corresponds roughly to the 20 dbZ radar reflectivity, or a rain rate on the order of 0.6 $mm \cdot h^{-1}$. Both of these studies suggest that the non-precipitating cloud liquid water content at zero rainfall rate should be significantly greater than the 0.057 gm m^{-3} derived from the Ridout simulation.

A simple modification of (3.1) resulted in liquid water contents more compatible with the base state model, with the previous hurricane simulations by Olson (1989), and with the composite Doppler radar studies of Hane, *et al.* (1982). Moreover this modification led to retrieved rain accumulations very similar to the Global Precipitation Index (Arkin, 1983; Hinton, 1987) estimates over June of 1979 in the Indian Ocean. This change consisted of multiplying (3.1) by four to give (3.2), which is illustrated in Figure 3.4.

$$q_{cloud} = 0.228 + 0.276 \cdot \ln(R+1). \qquad (3.2)$$

Intensive field programs such as the Darwin TOGA experiment (Keenan et al., 1988) should, in the future, help to establish more accurate parameterizations relating non-precipitating and precipitating liquid water contents in tropical clouds. We have adopted the relation (3.2) with the belief that it is at least reasonably consistent with current studies.

3.1.4 Integrations of $T_B(R)$ over rain rate distributions.

The model development so far has focussed on the simulation of radiances upwelling from plane-parallel (horizontally homogeneous) rain clouds. (See Figs. 3.1 and 3.2.) If a given SMMR field of view is subdivided into small areas over which the rain rate is nearly uniform, then we can use the plane-parallel radiative model to compute the radiance upwelling from each small area as a function of the rain rate within the area. The SMMR-observed brightness temperature can be approximated as the integral of the modelled radiance contributions from all of the small areas within the field of view. Therefore, in order to account for the spatial non-homogeneity of rain and complete the SMMR brightness temperature model, the spatial distribution of rainfall rates within the SMMR field of view must be defined.

In an initial test we used the base state model curves, including 2K random noise, and an exponential distribution of random numbers for the rain rates. Thus we produced simulated rain fields with variability on area scales smaller than the smallest SMMR footprint. The areas of these sub-resolution elements were 98 km^2, just under 10 km by 10 km. In these cases, the distributions of field-of-view average brightness temperatures versus average rainfall rate did not follow any idealized curve (*i.e.*, a spread of brightness temperature values was obtained for each rain rate). This meant that in the context of simple, single-channel algorithms operating on a field of view by field of view basis, we could expect many SMMR measurements to yield ambiguous rain rate estimates.

An exponential distribution of rates has the attractive feature that the mean rate is the only parameter. Unfortunately, this distribution is not as realistic as the double exponential, log-normal or gamma distributions. We ultimately concluded that the Short (1988) and Short and North (1989) result, that the β and α parameters of the Γ-distribution are correlated, provides the best simple remedy, in that it preserves both realism and the one parameter advantage. The β and α parameters are related to μ, the mean of R and σ^2, the variance of R. Specifically,

$$\mu = \alpha\beta$$

and

$$\sigma^2 = \alpha\beta^2.$$

With these definitions the Γ-distribution is given by,

$$P(R) = \Gamma(\alpha)\ \beta^{\alpha}\ R^{\alpha-1}\ \exp(-R/\beta). \qquad (3.3)$$

We define area-averaged brightness temperature, $<T_B>$, in terms of area-averaged rainfall rate, $<R>$, as follows. $T_B(R)$ is calculated from the radiative cloud model. P(R) is a Γ-distribution with $\beta = 10$, $\alpha\beta = <R>$ (Short, 1988).

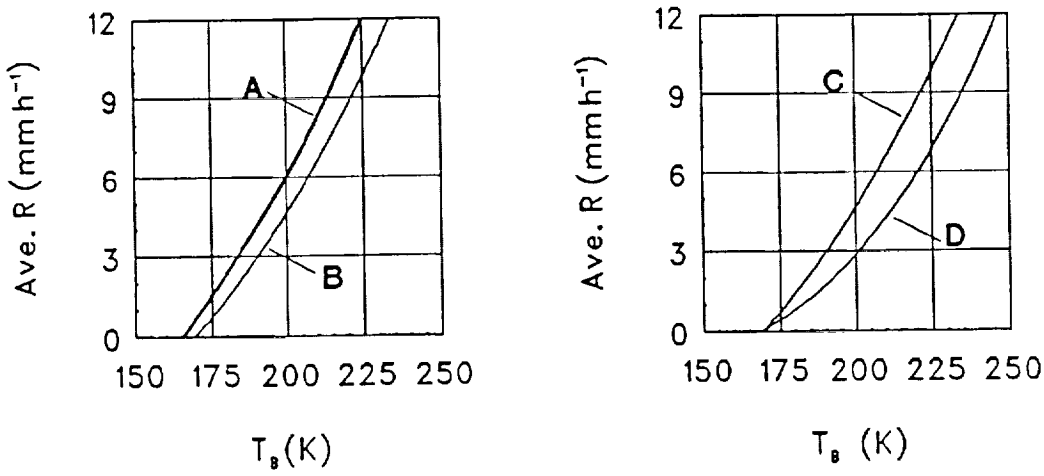

FIG. 3.6 Area averaged rain rate as a function of area averaged brightness temperature. The panel at left shows the relation for Γ-distributed rain rates and (A) 1 and (B) 4× our fit to Ridout's cloud model results. The relations on the right compare the Γ-distribution, (C), with an exponential distribution, (D) –both for 4× the cloud model-derived liquid water curve.

$$<T_B> = \int T_B(R) \cdot P(R) \cdot dR. \qquad (3.4)$$

$$<R> = \int R \cdot P(R) \cdot dR. \qquad (3.5)$$

Figure 3.6 illustrates the effect of the integrations (3.4) and (3.5) for one channel. The figure also shows average brightness temperature as a function of average rain rate for two non-precipitating liquid concentrations. It is from these mean values (equations (3.4) and (3.5)), rather than $T_B(R)$, that the rainfall algorithms are constructed.

3.2 One channel algorithms

In this section we consider the model results for the first time in "inverse" form, $<R>$ as a function of $<T_B>$. For simplicity, we will drop the $<...>$ notation for averages, as well as the subscript-B for brightness temperatures. This allows subscripts to designate various frequency and polarization channels.

Assume that in a field of view where it is raining with a mean rate μ, the probability density function for rain rate is given by (3.3) for $\beta = 10$. Further, assume the Ridout variation of non precipitating liquid water augmented by a factor of four. Then, we obtain the representations in Table 3.3 for rain rate as a function of brightness temperature for each channel.

The equations in Table 3.3 follow from polynomial regression of the average rainfall rate against the average model brightness temperature. Plots of the regression curves are presented in Figure 3.7. If these plots are compared with those of Fig. 3.1 (allowing for the rotation of axes and change of scale) it can be seen that the variations of brightness temperature with rain rate have retained some of their general characteristics. Nevertheless the changes in the curves amount to substantial changes in rain rate for a

given brightness temperature. This is most easily seen at 37 GHz. After integration (Fig. 3.7) the curves for 37V and 37H do not reach saturation at extremely low values of R as they do in Fig. 3.1.

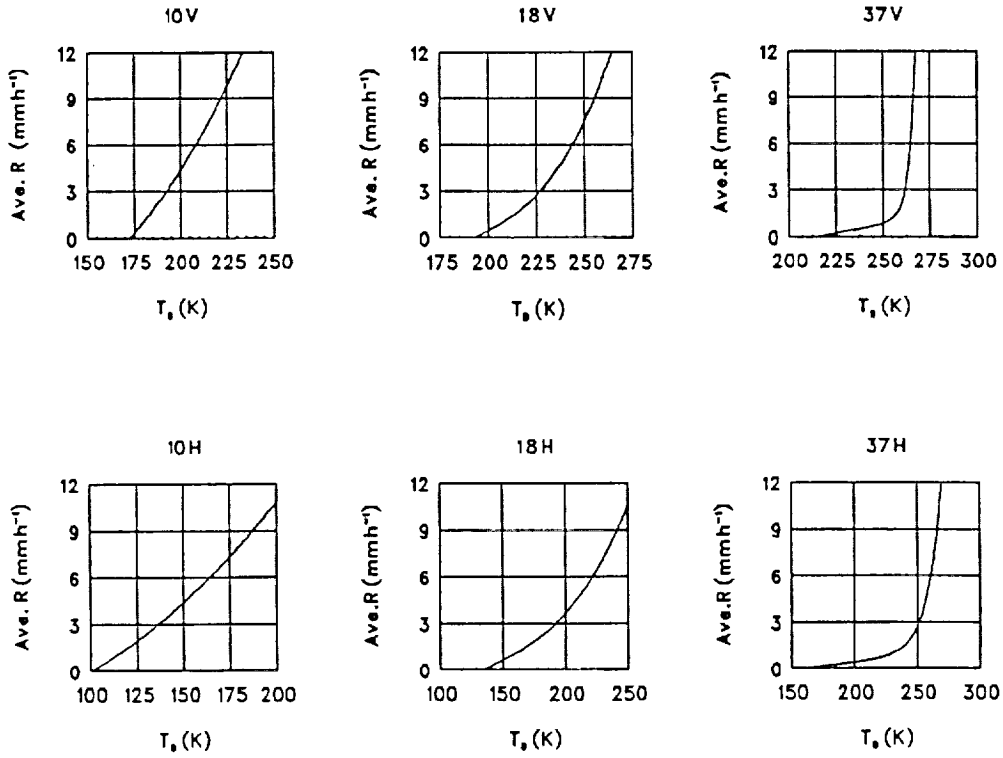

FIG. 3.7 Mean rain rate as a function of brightness temperature.

TABLE 3.3. Single channel algorithms. Mean rain rates as functions of brightness temperature for six SMMR channels, 10.7, 18 and 37 GHz.

Channel	Expression or Value	Break Points
R_{V10} =	0	$T_{V10} \leq 172.153$
	$0.12217 \cdot (T_{V10}-172.153) + 0.001118 \cdot (T_{V10}-172.153)^2$	$T_{V10} > 172.153$
	12	$R_{V10} > 12$
	0	$R_{V10} < 0$
R_{H10} =	0	$T_{H10} \leq 100.479$
	$0.06920 \cdot (T_{H10}-100.479) + 0.000395 \cdot (T_{H10}-100.479)^2$	$T_{H10} > 100.479$
	12	$R_{H10} > 12$
	0	$R_{H10} < 0$
R_{V18} =	0	$T_{V18} \leq 192.283$
	$0.06295 \cdot (T_{V18}-192.283) + 0.00002 \cdot (T_{V18}-192.283)^3$	$T_{V18} > 192.283$
	12	$R_{V18} > 12$
	0	$R_{V18} < 0$
R_{H18} =	0	$T_{H18} \leq 133.763$
	$0.038162 \cdot (T_{H18}-133.763) + 3.8664 \cdot 10^{-6}(T_{H18}-133.763)^3$	$T_{H18} > 133.763$
	12	$R_{H18} > 12$
	0	$R_{H18} < 0$
R_{V37} =	0	$T_{V37} \leq 213.38$
	$-5.0199 + (0.02333 \cdot T_{V37}) + \{0.6272 \cdot \exp[(T_{V37}-258)/3.3655]\}$	$T_{V37} > 213.38$
	12	$R_{V37} > 12$
	0	$R_{V37} < 0$
R_{H37} =	0	$T_{H37} \leq 159.42$
	$-1.3973 + (0.008942 \cdot T_{H37}) + \{3.8394 \cdot \exp[(T_{H37}-258)/11.0530]\}$	$T_{H37} > 159.42$
	12	$R_{H37} > 12$
	0	$R_{H37} < 0$

3.3 Multi-channel algorithm

A multi-channel rain rate estimate can be formed from the set, $\{R_{V10}, ..., R_{H37}\}$, of single-channel estimates given above. The multi-channel estimate is specified as the weighted average of the single-channel estimates using a set of weights, $\{W_{V10}, ..., W_{H37}\}$. The optimum estimate weighs the single-channel estimates by the inverses of their variances. Since these are not known *a priori* the variances must be approximated from,

$$(\delta R_{V10})^2 = (\partial R_{V10}/\partial T_{V10})^2 \cdot (\delta T_{V10})^2$$
$$\cdots$$
$$(\delta R_{H37})^2 = (\partial R_{H37}/\partial T_{V37})^2 \cdot (\delta T_{H37})^2$$

where the $\partial R/\partial T$ are obtained from the model studies for each channel.

If measurement errors are assumed to be independent and random, it follows that the single-channel weights are proportional to the inverse squares of the derivatives of R with respect to the brightness temperatures times the error variance for each channel.

$$W_{V10} \propto (\partial R_{V10}/\partial T_{V10})^{-2} \cdot (\delta T_{V10})^{-2}_{noise}$$
$$\cdots$$
$$W_{H37} \propto (\partial R_{H37}/\partial T_{V37})^{-2} \cdot (\delta T_{H37})^{-2}_{noise}$$

In the Nimbus-7 User's Guide (Gloersen and Hardis, 1978) a rms ΔT of <2 K is specified for all the SMMR channels. If the simplifying assumption is made that all the measurement errors are equal, then

$$W_{V10} \propto (\partial R_{V10}/\partial T_{V10})^{-2}$$
$$\cdots$$
$$W_{H37} \propto (\partial R_{H37}/\partial T_{V37})^{-2}$$

An examination of a plot of these weighting functions in Fig. 3.8 suggests that the 37 GHz channels (especially 37H) are most useful for rain rate estimation relative to the other channels below about 1 $mm \cdot h^{-1}$. Generally the H-polarized channels are much more significant than the V-polarized channels for each frequency.

There is a peak in the H18 GHz contribution from 1 to 5 $mm \cdot h^{-1}$, where its relative weight maximizes and dominates the other channels, as envisioned by Hinton and Olson (1988). However, V18 GHz does not participate in this dominance: although the V18 weighting function has almost the same shape as the H18 function, the overall magnitude of the V18 weighting is relatively small. Similarly, as expected, at higher rain rates the H10.7 GHz weighting dominates, though V10.7 (which has a weighting function with much the same shape as H10.7) is everywhere less than H18 weighting. On the other hand, everywhere above 2 $mm \cdot h^{-1}$ V10.7's weighting is certainly large enough to contribute to the multi-channel rain rate estimate.

In the rain rate region between 2 and 6 $mm \cdot h^{-1}$ the H10.7 GHz and H18 GHz channels should yield the most rain rate information, while the important rain/no-rain and very low rain rate discrimination requires the H37 GHz channel. It is convenient to have simple analytical representations of the weights, as given by the regression relationships in Eq. (3.6). These relationships are illustrated in Figure 3.8. The final rain rate retrieval estimate is given by the weighted average of the single-channel rain rate estimates from Table 3.3, weighted by the factors in Eq. 3.6.

$$
\begin{aligned}
W_{V10} &= 0.182 \cdot [1 - \exp(-0.257 \cdot R_{V10})] \\
W_{H10} &= 0.493 \cdot [1 - \exp(-0.257 \cdot R_{H10})] \\
W_{V18} &= 0.175 \cdot [1 - \exp(-1.53 \cdot R_{V18})] \cdot [\exp(-.0717 \cdot R_{V18})] \\
W_{H18} &= 0.516 \cdot [1 - \exp(-1.39 \cdot R_{H18})] \cdot [\exp(-.0698 \cdot R_{H18})] \\
W_{V37} &= 0.004 + 0.125 \cdot \exp(-R_{V37}) \\
W_{H37} &= 0.019 + 0.776 \cdot \exp(-R_{H37})
\end{aligned}
\qquad (3.6)
$$

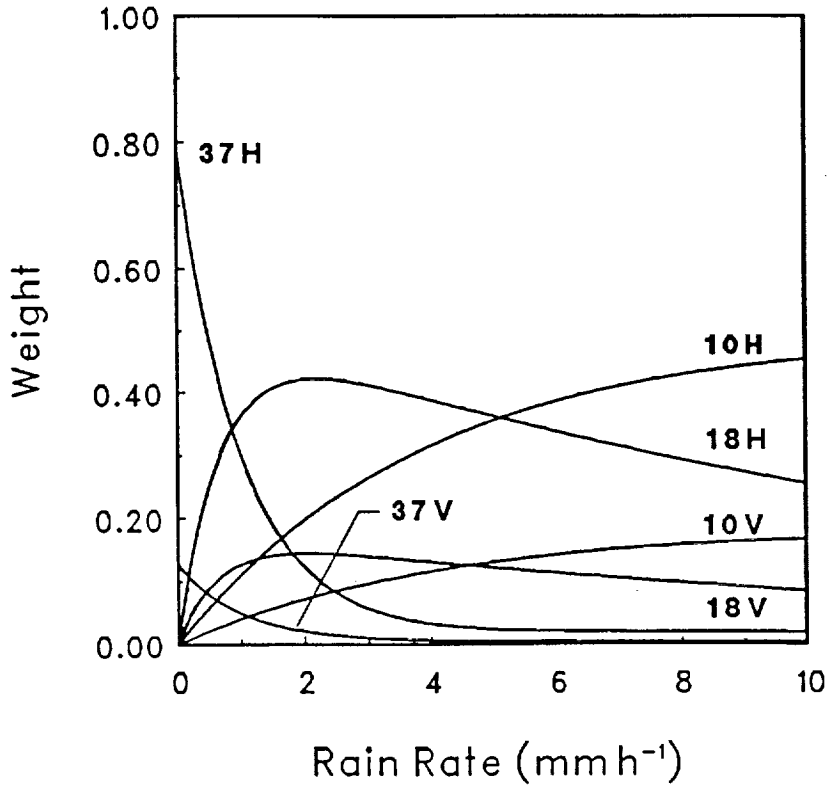

FIG. 3.8 Idealized weights for SMMR channels 10.7 through 37 GHz, H- and V-polarization.

4.0 SMMR RAINFALL

4.1. Data Processing

SMMR data were processed in two steps. First, on an IBM 4381 mainframe and building on software available from the Man-computer Interactive Data Access System (McIDAS), we carefully renavigated the SMMR data and then gridded them over one-quarter degree boxes. The area of such a grid box is comparable to that of the footprint of a 37 GHz channel. These grids were stored on magnetic tape for later input into the coded algorithm.

In the second stage, the multi-channel algorithm as described in the previous section was used on the quarter degree grid data to compute the actual rain amounts on a monthly basis over a one degree grid, using an IBM PC. These rainfalls were printed out and inspected for processing errors. In particular, the land areas, which produced "rainfall" far in excess of the ocean areas, stood out clearly and allowed an easy check for navigation errors (a misalignment of the SMMR grids would blur the coastline edge). Additional information collected on each monthly rainfall grid included a list of all SMMR passes being used as input and a map of N, the number of observations each month over a grid box. An example of the N map for November 1979 is shown in Figure 4.1. The sharp gradient of N near the southern boundary of the analysis area is not due to the actual cessation of SMMR observations in that region, but the effect, rather, of our terminating the input of SMMR data around 26°S.

Production of the contoured rainfall maps made use of an IBM PS/2 Model 70 and HP Laserjet Printer Series II along with the IUR Meteorological Analysis Graphics Package developed at SSEC. The objective analysis is based on the Barnes scheme. Before the fields were contoured, land and island areas were masked. Missing data areas along the very edge of the analysis area were also excluded.

The algorithm was applied to SMMR data from the period 1 December 1978 through 31 December 1981. Analyses to follow concentrate on the years 1979, 1980 and 1981. First we evaluate the algorithm and then present a summary of Indian Ocean rainfall over the three years.

4.2 Evaluation of the Algorithm

The aim of the evaluation is to assess at first-order level the performance of the algorithm on large-synoptic and climatic scales. We attempt this assessment through comparisons of the UW SMMR rainfalls with climatologies of rainfall and with certain limited measurements of rainfall.

4.2.1 Verification Data

One of the glories of Indian Ocean meteorology is the ingenuity expressed in efforts through the years to infer the ocean's rainfall. Apart from gauges and SMMR itself, these inferences have been based on ship reports of present weather and on satellite observations at visible and infrared as well as millimeter wavelengths. The present evaluation draws on a number of these sources.

Ideally we should have a long series of monthly rainfalls over some representative part of the ocean for this evaluation. The area of the measurements would be of the order of several 10.7 GHz footprints, *i.e.* $5 \cdot 10^5$ km^2; the period, at least a year; the dates, 1979, 1980 or 1981. Coinciding observations of sea surface temperature, wind speed, water vapor as a function of height above the sea, cloud type and cloud amount are not as important, but nevertheless would be useful.

What is available to us falls far short of the ideal. Surface-based information on maritime rainfall is contained in maps and atlases presented by Dorman (1982), Geiger (1965) and Shea (1986). The periods of these mappings are long compared to that of the UW mapping (Table 4.1). Only one--that of Shea--overlaps ours.

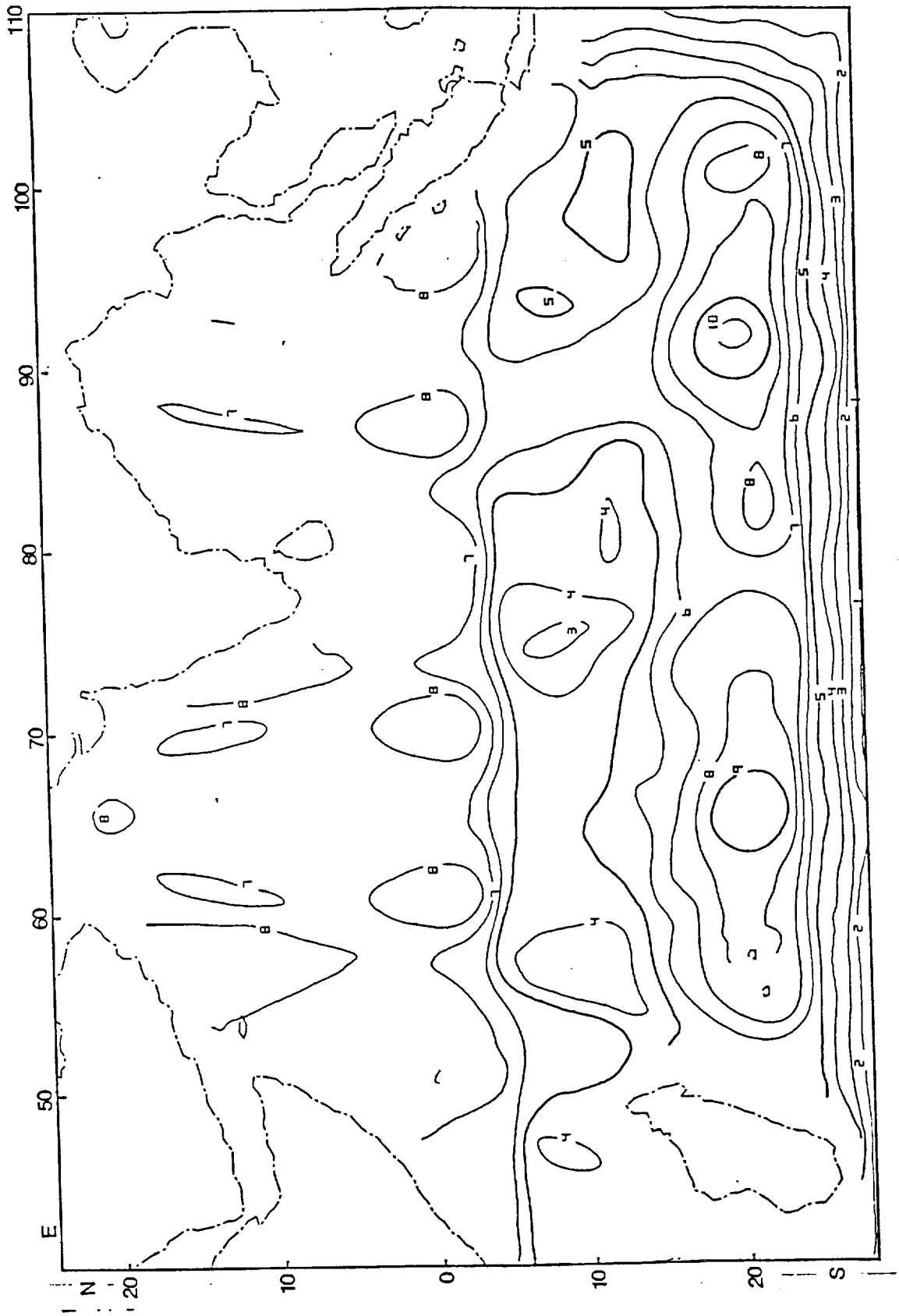

FIG. 4.1 Contour plot of the number of SMMR passes contributing to the calculation of rainfall at each grid point for November, 1979.

Additionally, through Philip Arkin we have India Meteorological Department gauge rainfalls for the months of the southwest monsoon (June, July, August and September), including the three years of the present analysis. The time resolution of these rainfalls is one week. Individual gauge reports had been averaged according to meteorological provinces called subdivisions (e.g., see Mooley and Shukla, 1987). Subdivisions include one, the Laccadive Islands, which may be considered representative of the open ocean. One other subdivision, the Andaman/Nicobar Islands, is surrounded by water. Otherwise, eight subdivisions have more or less extensive coastlines (Figure 4.2). Gauges may number as few as two or three for each of the island subdivisions.

TABLE 4.1. Characteristics of climatological mappings of Indian Ocean Rainfall

Property	Author		
	Dorman	Geiger	Shea
Dates	1950-74	Pre-Depression	1950-79
Period (years)	25	Many	30
Platforms			
Ships	Y	Y	Y
Land (inc. islands)	N	Y	Y
Reports			
Raingauge	N	Y	Y
Present Weather	Y	Y	N
Analysis Resolution			
Month	N	N	Y
Season	N	N	Y
Year	Y	Y	Y
Latitude (deg.)	2	~5	2.5
Longitude (deg.)	5	~5	2.5

4.2.2 Analysis

UW rainfalls are compared with these climatological mappings through profiles along two eastern meridians, the sixty-fifth and the ninetieth. The sixty-fifth meridian bisects the

Arabian Sea; the ninetieth meridian bisects the Bay of Bengal. All rainfalls are annual values; however, the resolution of the mappings varies from one to several degrees in latitude and longitude.

Along the sixty-fifth meridian (Figure 4.3a), UW rainfall follows trends in the climatological mappings and closely matches amounts at both ends of the section. But in the middle of the section the UW curve defines the lower envelope of curves. The disparity is greatest at the rainfall peak (near 5°S), where UW rainfall is about 70% of Geiger and Shea's rainfall and less than half Dorman's rainfall. The UW curve also exhibits more structure than the climatological curves; in particular, a secondary peak over the Arabian Sea.

Along the ninetieth meridian (Fig. 4.3b) all curves show significant peak rainfalls between 3° and 5°S. At the northern (Bay of Bengal) end of the section, UW rainfall is two-thirds of climatological rainfalls. Otherwise, in spite of a rather different envelope of profiles, the relationships found for the sixty-fifth meridian hold also for the ninetieth meridian.

The profile comparisons assure us that the UW estimates are not inconsistent with existing climatologies of Indian Ocean rainfall. At the same time they indicate that the UW estimates may carry a low bias. To take the evaluation one step further, we compare the UW estimates of rainfall with the Arkin set of gauge measurements.

We tentatively suppose that coastal and island subdivision rainfall reflects (marine) rainfall in nearby UW boxes. As the distance between a subdivision and a box increases, the association weakens. We do not expect rainfall from inland subdivisions to bear any useful relationship to marine rainfall. Even for islands, where diurnal forcing of convective rainfall may be relatively weak, it is likely that on the whole subdivision rainfall will exceed UW rainfall (e.g., see Kilonsky and Ramage, 1976).

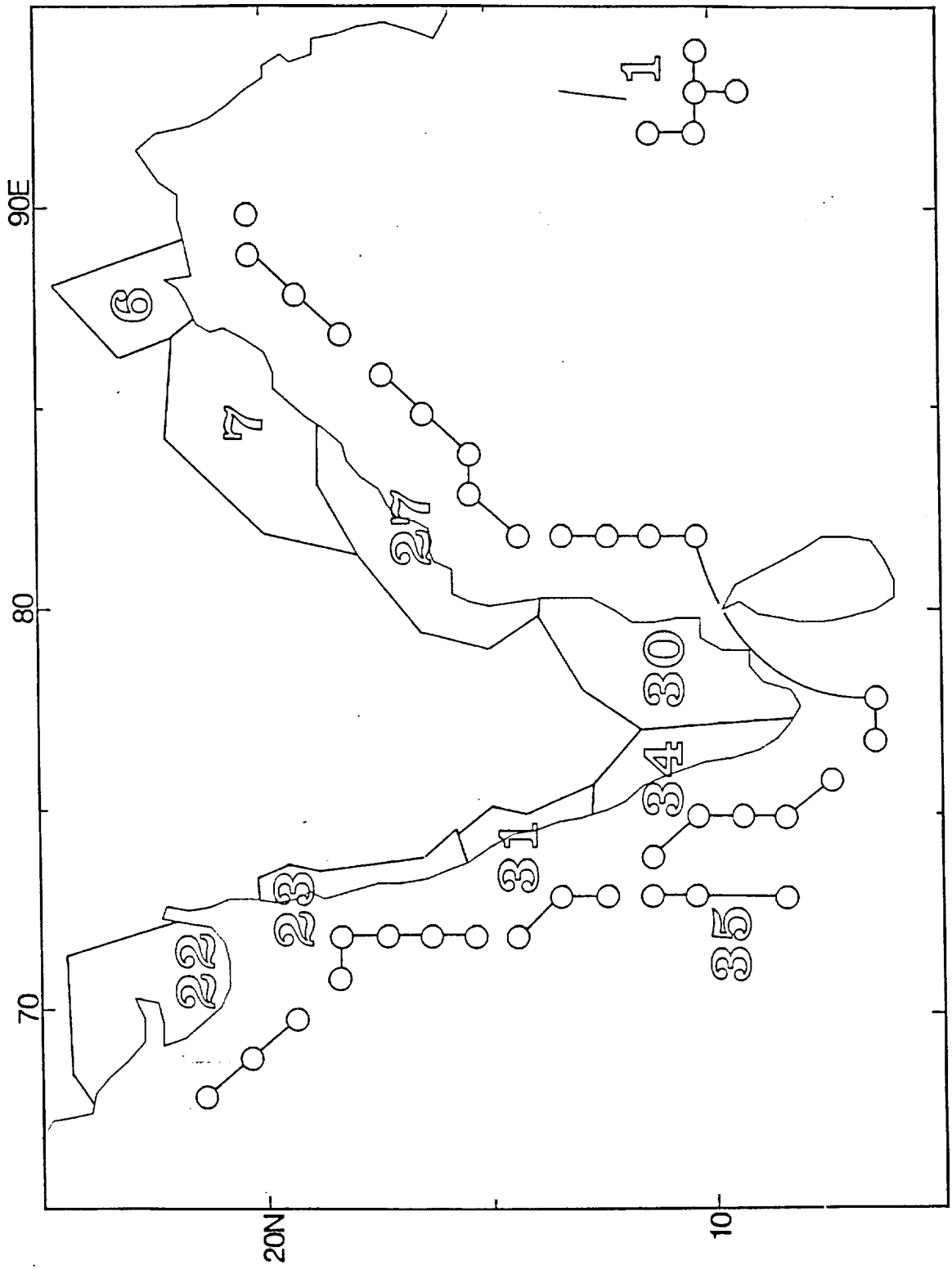

FIG. 4.2 Rainfall subdivisions and clusters of SMMR grid boxes used in the algorithm evaluation. Numbers correspond to individual subdivisions. Circles mark the centers of grid boxes. Lines connect those boxes which are associated with a particular subdivision.

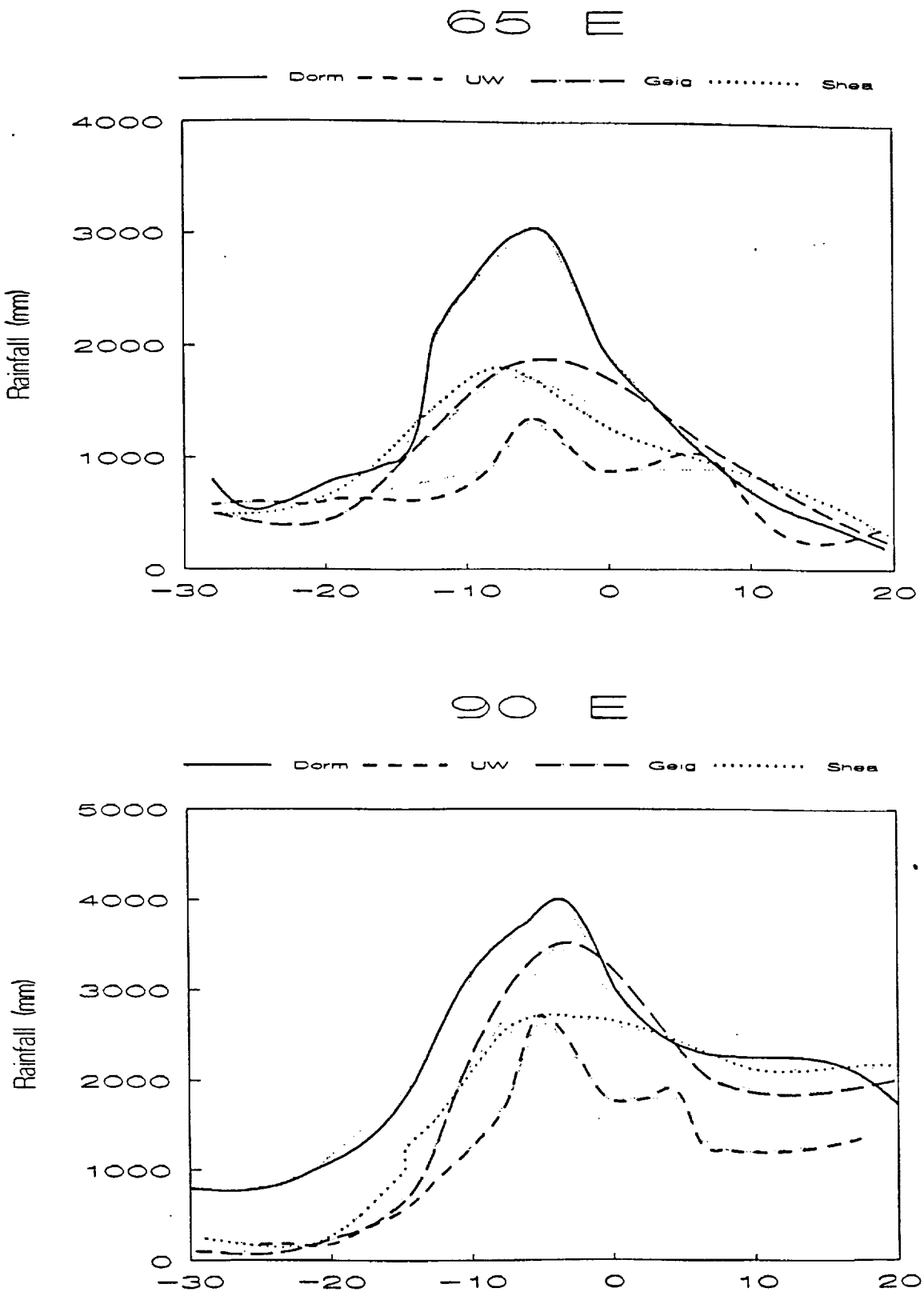

FIG. 4.3 Latitudinal profiles of average annual rainfall over the Indian Ocean. In addition to the present analysis, the three mappings represented are Dorman, Geiger, and Shes. (see Table 4.1)

These considerations lead us to associate abutting (or, for island subdivisions, surrounding) boxes with subdivision rainfall. The average of rainfall for the cluster of boxes facing each subdivision is compared with subdivision rainfall. The locations of boxes as well as the boundaries of subdivisions are shown in Figure 4.2. To be consistent with another analysis, which is described below, the comparison is limited to June, July and August. Accumulations of rain for each of these months through each of the three years differ slightly in respect to period. For UW rainfalls, they correspond exactly to calendar dates. For subdivision rainfalls, accumulations correspond to the nearest weeks, such that only weeks falling one half or more in a month contribute to that month's rainfall.

For the entire sample of 90 points (ten subdivisions, three months, three years), the mean of UW rainfall came to 70% of the mean of subdivision rainfall (Table 4.2). As might be expected of a parameter which is inherently areal, the variance and range of UW rainfalls both are smaller than corresponding values for subdivision rainfalls.

TABLE 4.2. UW (SMMR) and subdivision (gauge) monthly rainfall. The period covered is June, July and August of 1979, 1980 and 1981. Units are $mm \cdot mo^{-1}$

Statistic	All Subdivisions (n=90)		Island Subdivisions (n=18)	
	SMMR	Gauge	SMMR	Gauge
Mean	26.3	37.4	21.8	32.2
Median	23.1	30.1	20.0	28.6
Standard Deviation	14.7	29.8	9.3	20.2
Minimum	6.1	1.8	6.1	12.5
Maximum	81.7	126.2	42.5	91.7

Treating the two island subdivisions separately from the coastal subdivisions does little to change the ratio of the means. Only in respect to the absolute minimum monthly rainfall is there any change in the relationships of the other statistics.

Pairs of points for the full sample are shown in Figure 4.4. Apart from the tendency for subdivision rainfall to exceed UW rainfall, the plot indicates a positive association, but a large dispersion as well.

In Figure 4.5 the points are treated as two time series. Each series corresponds to one three-month season. Within 20%, absolute differences are uniform from year to year. However, differences are by no means uniform from subdivision to subdivision. UW rainfall tends to exceed gauge rainfall for the driest subdivisions; consistently, it falls below gauge rainfall for the wettest subdivisions. This shortfall is especially marked for the three subdivisions lying between the Western Ghats and the Arabian Sea (numbers 23, 31 and 34 in Figure 4.2). There UW rainfall averages 40% of subdivision rainfall. Such a result is generally consistent with climatologies of the frequency of rain over the Indian Ocean, e.g., those of Ramage (1984) or Hastenrath and Lamb (1979). For the boreal summer months, these show a gradient normal to India's west coast, but parallel to India's east coast.

TABLE 4.3. Regression analysis of subdivision and UW monthly rainfalls. Model is Y = a + bX, where X is subdivision rainfall and Y is UW rainfall.

Sample	a mm mo^{-1}	b	SEE mm mo^{-1}	ρ	ρ^2 %	n
All Subdivisions	20.9	0.14	14.2	0.29	8	90
Island Subdivisions	16.2	0.18	8.8	0.38	15	18

Note: SEE, the standard error of estimate, is defined as the square root of the mean squared error; ρ is the correlation coefficient.

A linear regression analysis, with UW rainfall as the dependent variable, yields the results shown in Table 4.3. The UW monthly rainfall and subdivision rainfall correlation is 0.29. If a 21 mm offset (gauge exceeding UW) is removed, in two-thirds of the cases UW monthly rainfall is within 14 mm of subdivision rainfall. In spite of drastically reduced numbers of gauges (as few as two or three per subdivision), for the two island subdivisions

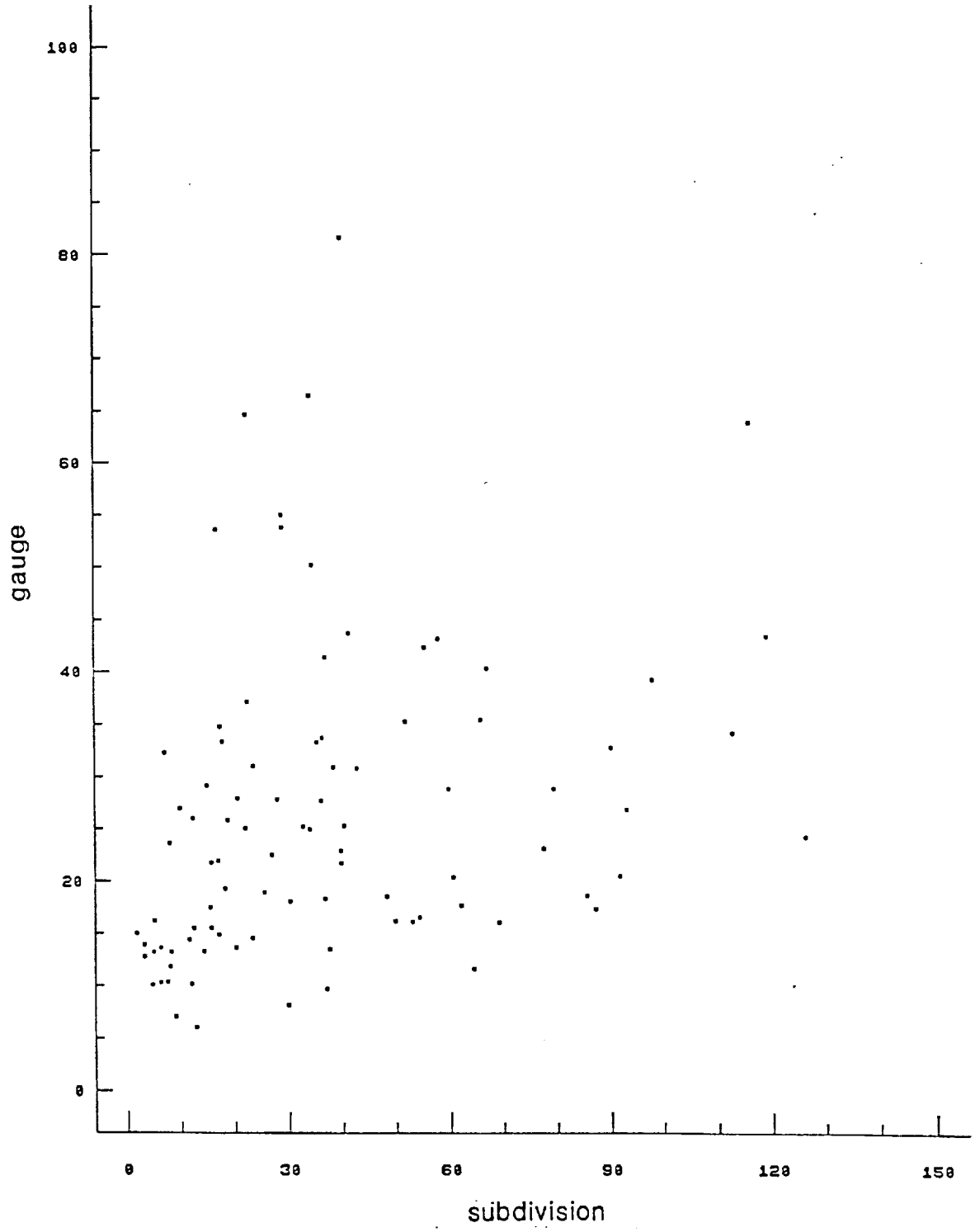

FIG. 4.4 Scatterplot of monthly subdivision rainfall and monthly UW (SMMR) rainfall, all subdivisions. Units are centimeters.

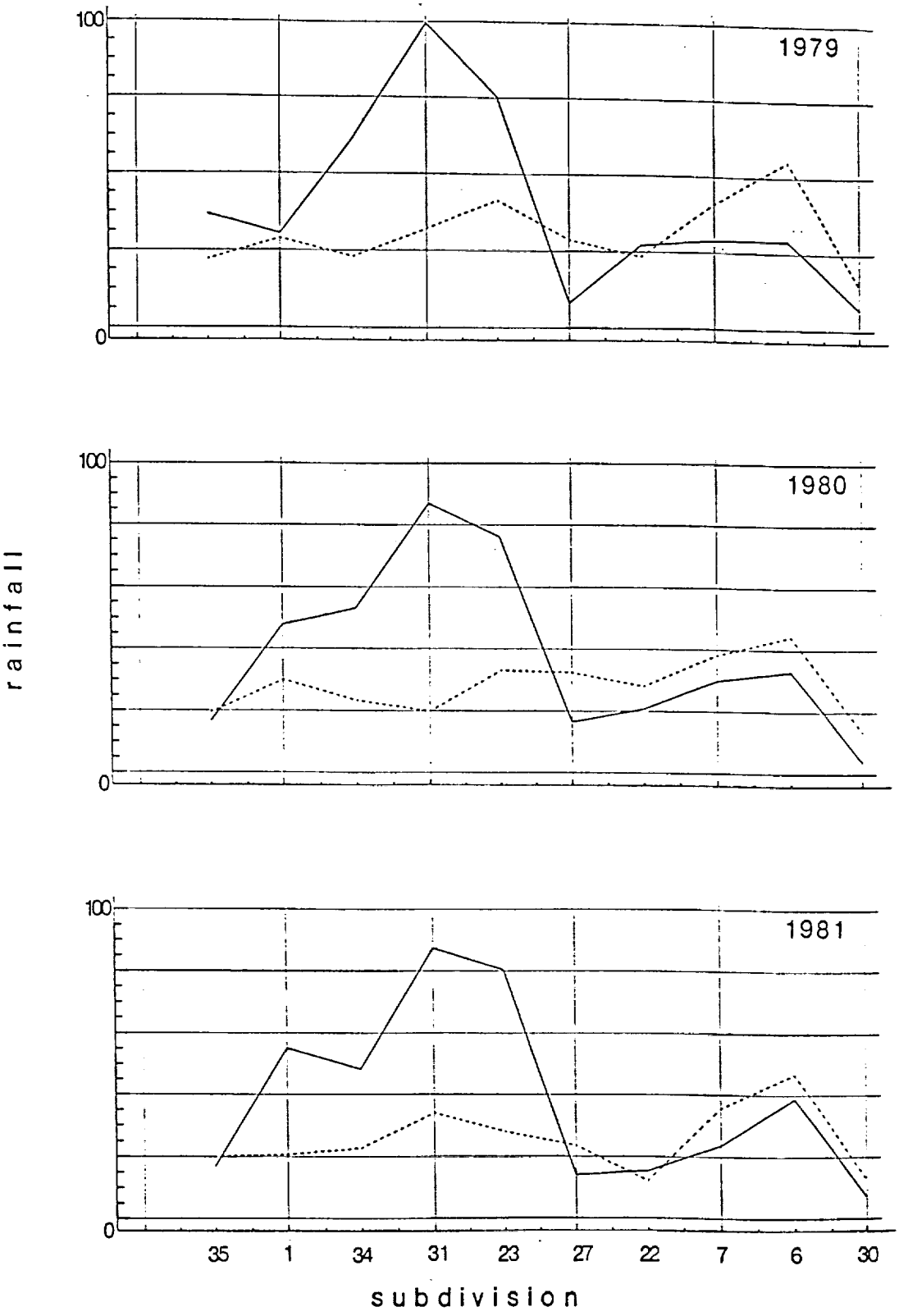

FIG. 4.5 Subdivision and UW monthly rainfalls plotted as a time series. Points 1 through 30 correspond t 1979, 31 through 60 to 1980, 61 through 90 to 1981. Within years, points are ordered (according to subdivision) as 35, 1, 34, 31, 23, 27, 22, 7, 6, and 30.

alone the correlation rises to 0.38, the offset shrinks to 16 mm and the standard error of estimate drops to 9 mm.

Thus the subdivision analysis supports both findings of the climatology analysis. The UW algorithm is responsive to rain over the Indian Ocean; however, its estimates tend to be low.

There are two satellite-microwave mappings for which comparisons also are possible. The first is that of Rao *et al.* (1976); the second, that of Prabhakara *et al.* (1986). The mapping of Rao *et al.* draws on observations of an early instrument, the Electrically Scanning Microwave Radiometer (ESMR). It covers two years, 1973 and 1974, at a resolution of four degrees in latitude and five degrees in longitude. The mapping of Prabhakara *et al.* draws on observations of SMMR. It covers six months of our own analysis, December 1978 through February 1979 and June through August 1979, at a resolution of 1.4 degrees in latitude and longitude.

In each case we compare mappings by means of profiles along the sixty-fifth and ninetieth meridians as well as certain areal statistics.

Annual (1973) profiles from Rao *et al.* (1976) are shown in Figure 4.6. UW (1979-1981) rainfall is lower at the heads of both the Arabian Sea and Bay of Bengal. The UW profiles also show much more structure. Otherwise, given differences in the averaging periods, the two pairs of curves are in remarkable agreement.

Annual rainfall averaged over the basin is in similar agreement. For the purpose of this comparison, "basin" is equivalent to the UW domain, *i.e.*, open-ocean areas between the eastern meridians, 40.5° and 110°, and north of the southern parallel, 28°. Only the Rao *et al.* grid boxes more or less wholly within that domain were candidates for the comparison. For 1973 the average of Rao *et al.* rainfall over this area, comprising 113 grid boxes, is 1008 mm (Table 4.4); that of UW 1979-1981 rainfall, comprising an average of 2492 grid boxes, is 919 mm.

TABLE 4.4. Microwave estimates of rainfall over the Indian Ocean

Statistic	Estimates Previous	Present
Area Average (mm yr^{-1})	1008[1]	919[2]
Area of 427 mm (3 mo)$^{-1}$ contour (deg^2)		
Dec 78 - Feb 79	784[3]	400
Jun - Aug 79	700[3]	325

1. Rainfall is calculated from Rao *et al.* (1976) for 1973;
2. Period is 1979-1981;
3. Area is measured from Fig. 2 in Prabhakara *et al.* (1986).

Profiles from Prabhakara *et al.* (1986) are shown in Figure 4.7. Along the sixty-fifth meridian (Figure 4.7a), UW rainfall tends to fall short of Prabhakara *et al.* rainfall. The difference is especially noticeable in curves for the boreal winter months (December, January and February), across the peak near 10°S. Otherwise, both sets of curves are in quite good agreement.

Along the ninetieth meridian (Figure 4.7b), differences are larger. In the Bay of Bengal as well as across the near-equatorial peak, UW rainfall is 300 to 400 mm below Prabhakara rainfall.

The systematic difference which the profiles imply is supported by a calculation of rain area. The threshold used in the calculation is 427 mm, a value which (by Equation 5 in Prabhakara *et al.*) corresponds to the 8 gm cm^{-2} contour of column-integrated liquid water in Figure 2 of Prabhakara *et al.* This threshold represents a fairly heavy rain rate (nearly half a centimeter per day or more than one and one-half meters per year). For the boreal winter, rain area so defined was measured on the map of Prabhakara *et al.* to be 780 deg^2, nearly twice the value calculated for the corresponding UW map (Table 4.4). For the boreal summer, the ratio of areas (Prabhakara to UW) was even larger.

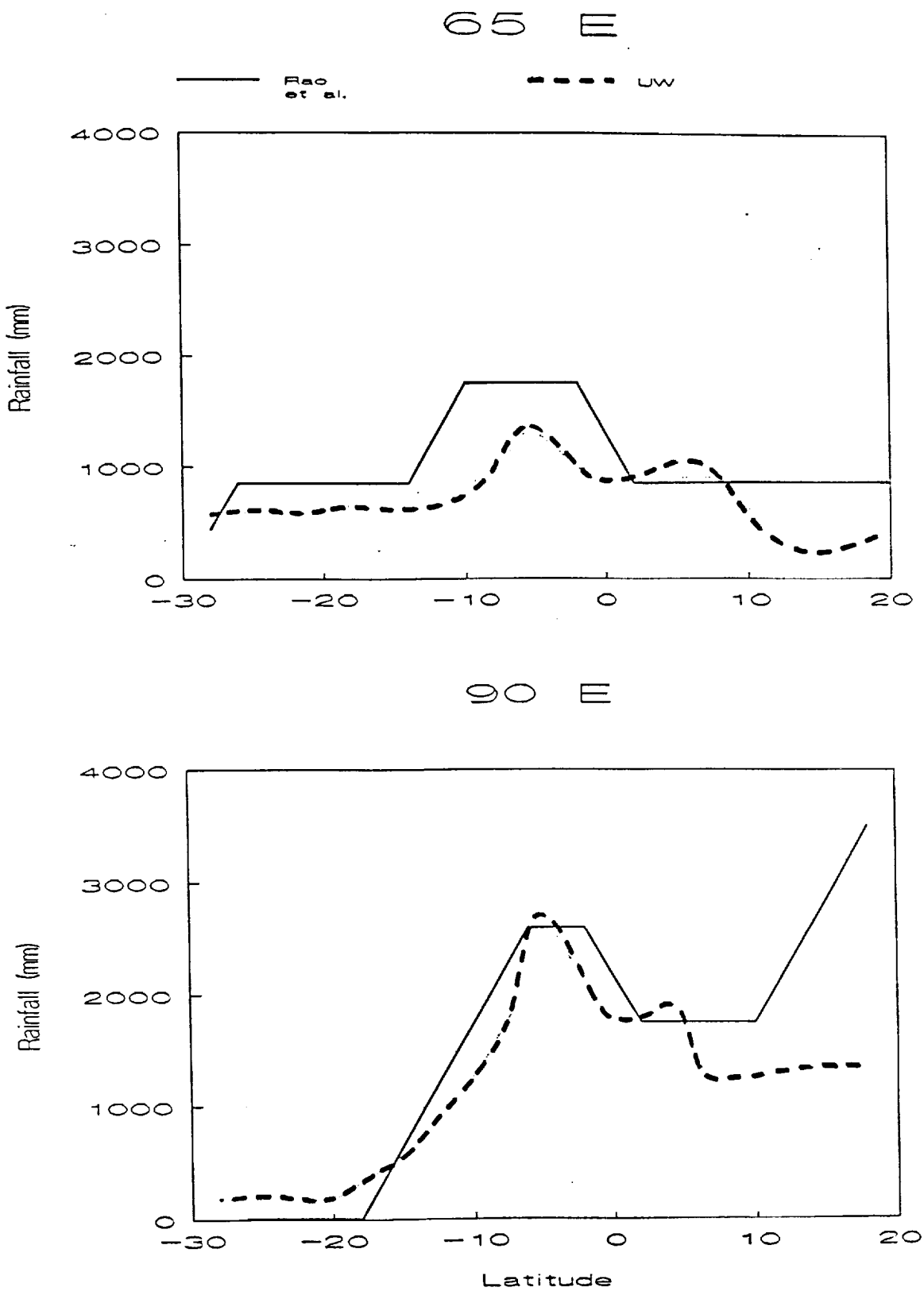

FIG. 4.6 Latitudinal profiles of annual rainfall over the Indian Ocean according to Rao *et al.* (1976) and the present study. Curves for Rao *et al.* are for 1973; for UW, 1979-81.

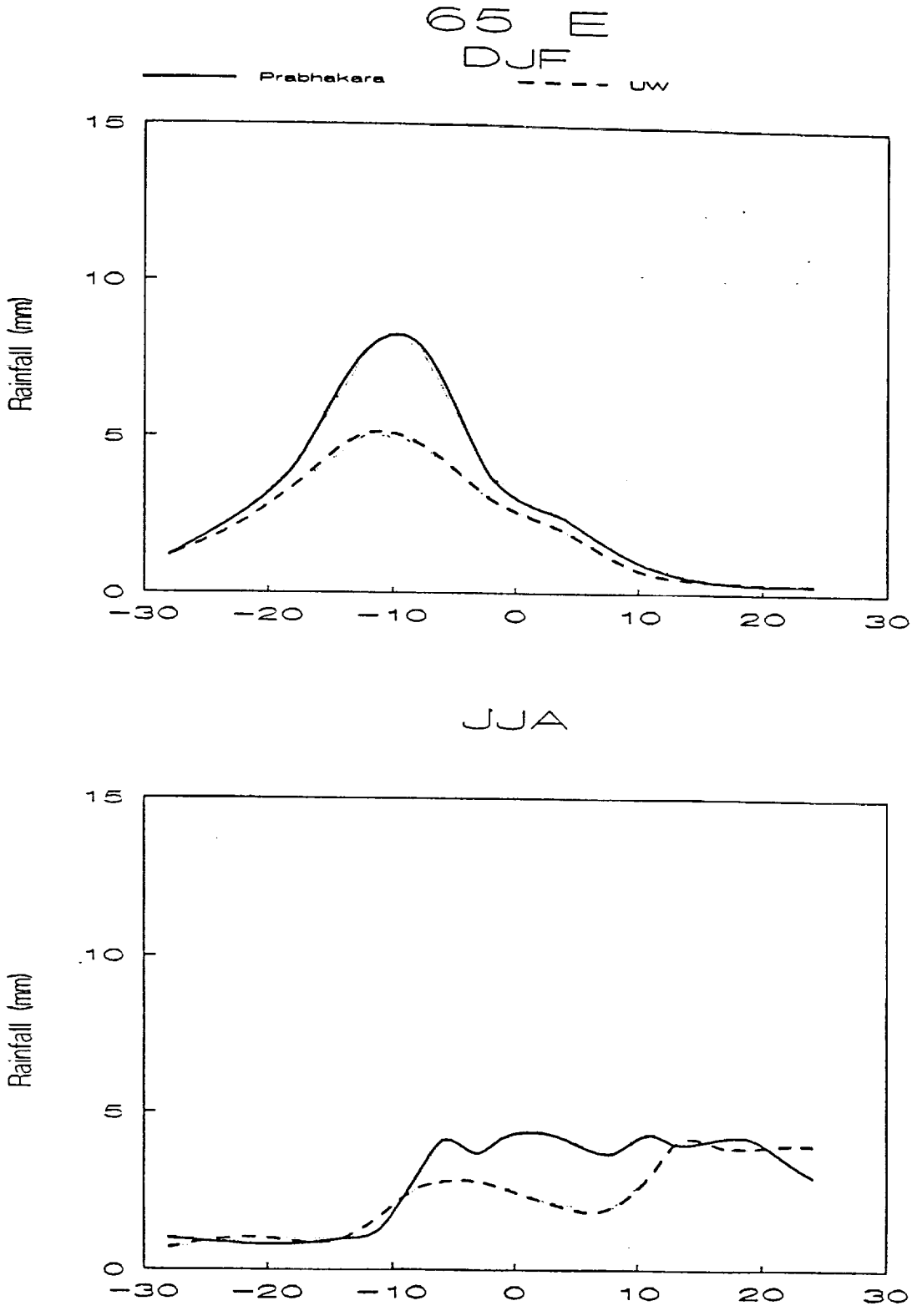

FIG. 4.7a 65°E latitudinal profiles of 1979 boreal winter (DJF) and boreal summer (JJA) rainfall over the Indian Ocean according to Prabhakara *et al.* (1986) and the present study.

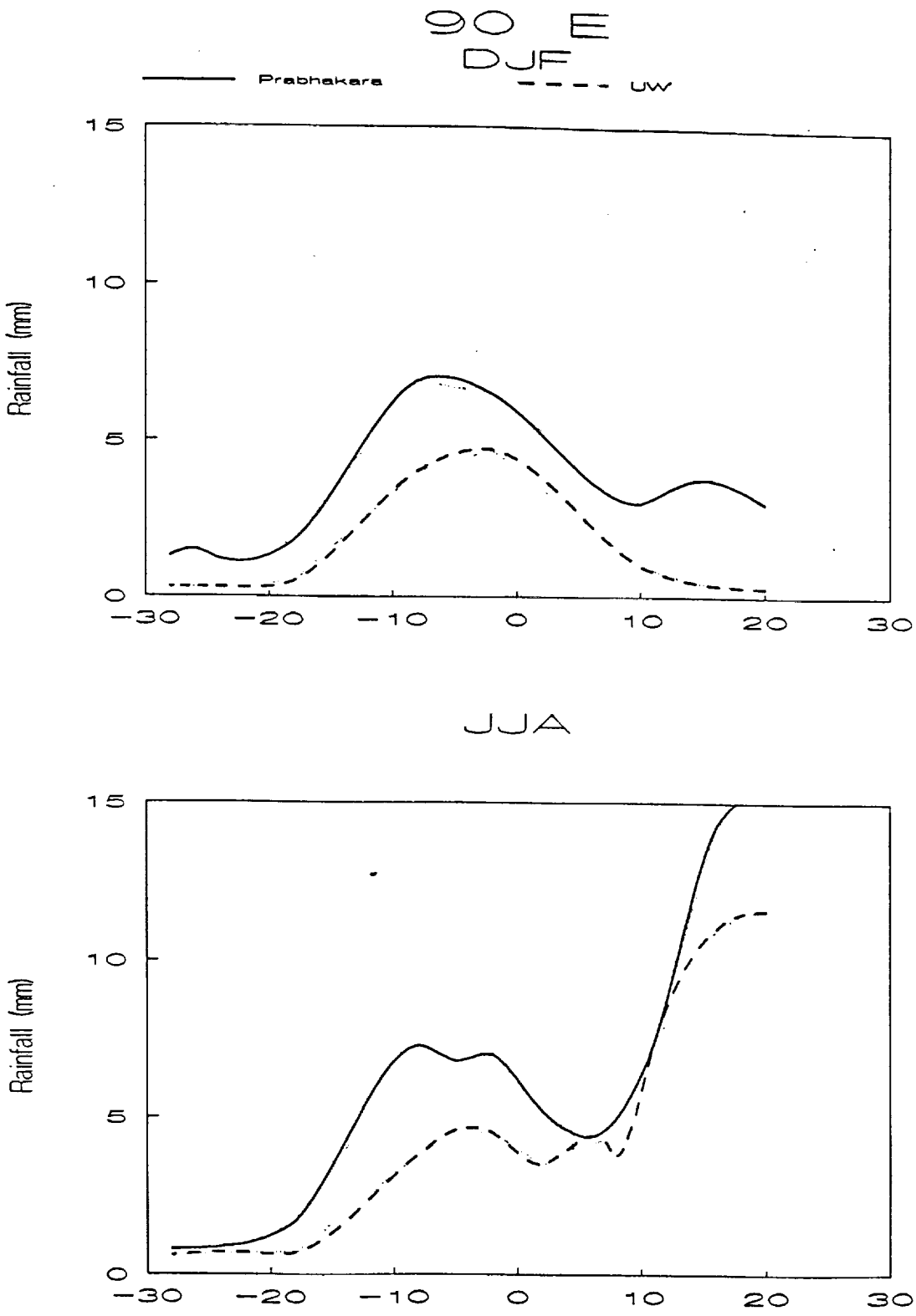

FIG. 4.7b Same as for Fig. 4.7a, except 90°E.

Uncertainties in the independent measurements, together with inconsistencies in the spatial and temporal sampling of rainfall, preclude sweeping generalizations about the UW algorithm. The weight of evidence does imply the presence of a small low bias. Nevertheless, over the Indian Ocean the algorithm appears to perform at least as well as published microwave algorithms.

The bias in the Indian Ocean rain estimates is quite sensitive to the chosen parameterization for non-precipitating liquid water (see section 3.1.3). The issue of the non-precipitating liquid is still not resolved. By varying the relationship of cloud liquid water to precipitation, agreement could be obtained with any one of the other estimates quoted above. But to do so would obscure the need for more research on this relation.

4.3 Indian Ocean Rainfall

If the context of this work is space technology, the driver is the Asian monsoon. That rainfall is central to the monsoon is a given. But most of what we know about monsoon rainfall comes from measurements made on land [e.g., see articles by Ananthakrishnan (1978), Mooley and Shukla (1987), Shukla (1987) and Hartmann and Michelsen (1989)]. By and large it is studies based on these measurements which define the principal issues of rainfall over the Indian Ocean. Limited as it is to three years of data gathered entirely from space, the present study cannot address all of these issues. Of those which can be addressed, the most noteworthy are as follows.

1. Is rainfall over the Ocean as variable as rainfall over the subcontinent?

2. Is the structure which is observed in rainfall along the coast part of a larger structure centered over the ocean?

3. Is boreal summer rain over the Arabian Sea significant?

With these questions in mind, in the paragraphs which follow we summarize the main results of the present mapping.

Over the Indian Ocean rainfall averaged just over 900 mm per year (Table 4.5). This is about 50 mm more than the long-term average annual rainfall over India south of the foothills of the Himalaya Mountains (Mooley and Shukla, 1987). Ocean-average rainfall proved to be remarkably consistent. Normalized by the mean, the range was a mere 3%. But for particular boxes variability was much greater. This is indicated in statistics of minima and maxima. Even for maximum values, the range exceeds 30% of the mean.

Very broadly, rain over the Indian Ocean fell in a diagonal belt trending northeast to southwest (Figure 4.8). Along the belt falls were heaviest--two to three times the mean--toward the east. Falls were less than half of the mean along the African and Arabian coasts of the Arabian Sea and less than one-fifth of the mean offshore from Australia.

TABLE 4.5. UW rainfalls: Annual averages in $mm \cdot yr^{-1}$.

Region	Statistic	Period			79-81
		1979	1980	1981	
Indian Ocean	Mean	907	936	915	919
	Minimum	24	67	9	67
	Maximum	3338	3196	4401	2946
Arabian Sea	Mean	766	686	722	725
Bay of Bengal	Mean	1559	1810	1689	1686

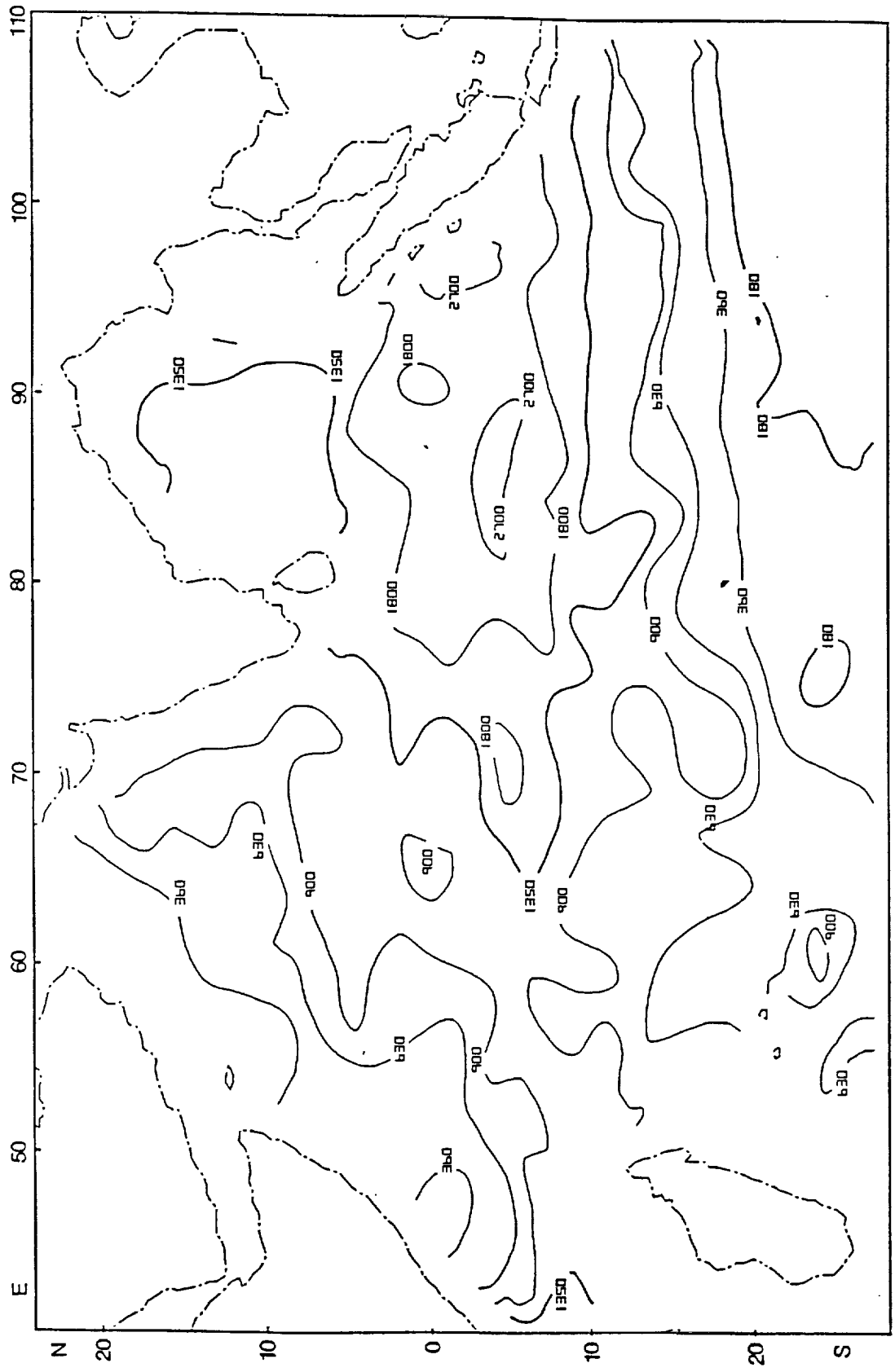

FIG. 4.8 1979-1981 annual average rainfall over the Indian Ocean. Units are millimeters.

Within the belt there is a tendency for rain to be organized into zonally-oriented bands. The most conspicuous of these bands spans the Ocean near 4°S. This near-equatorial rain axis is bounded to the south (near 24°) by a dry axis which extends to the west almost as far as the Mascarene Islands. A ridge and trough pattern exists over the Arabian Sea: trough along the equator, ridge near 5°N and trough extending southwest from Arabia. Taking account of rainfall over India (e.g., see Mooley and Shukla, 1987), we find that the Arabian trough rounds the tip of India and connects with a broad, shallow trough in the western half of the Bay of Bengal. It may be associated with the gradual spread of cooler water across the more northerly part of the Arabian Sea following the onset of the southwest monsoon (Saha, 1974; also see sea-surface temperature maps in Hastenrath and Lamb, 1979).

Changes from year to year are shown through departure maps in which the three-year average map is subtracted from each single year map. In 1979, a dry year for India (Mooley and Shukla, 1987), the near-equatorial rainfall axis was shifted from its average position (Figure 4.9a). Paradoxically, the shift was toward India rather than away. Apparently, this relatively modest displacement of the near-equatorial rainfall axis (two to three degrees of latitude) was accompanied by a corresponding displacement of the Arabian Sea/Bay of Bengal rainfall trough. Large negative anomalies in the central Bay and Head Bay suggest an extension of the trough as well.

Although not as well defined, anomaly patterns for 1980 (Figure 4.9b) oppose those of 1979. As in the case of 1980, during 1981 (Figure 4.9c) the near-equatorial rainfall axis was shifted slightly to the south. However, anomalies were positive over the Arabian Sea to the west of south India and over the Bay of Bengal to the east. Thus, there was no rainfall trough in Indian longitudes. Both years brought normal rains to India (Mooley and Shukla, 1987).

As Table 4.6 shows, over the Indian Ocean through the three years of the study, there was practically no difference between rainfall during the northeast monsoon months (December, January and February) and rainfall during the southwest monsoon months (June, July and August). From year to year the differences were somewhat greater, but no patterns are apparent.

TABLE 4.6. UW rainfalls: Seasonal averages in $mm \cdot mo^{-1}$.

Region	Dec - Feb				Jun - Aug			
	1978-79	1979-80	1980-81	1978-81	1979	1980	1981	79-81
Indian Ocean	83	82	65	77	73	80	71	75
Arabian Sea	47	30	23	33	47	97	79	92
Bay of Bengal	65	62	75	67	190	237	187	205

During the northeast monsoon season the near-equatorial axis of heavy rain was strong and somewhat south of its average position (Figure 4.10a). Although weak, it was still present during the southeast monsoon season (Figure 4.10b) and still lay south of the equator. A hint of a northern hemisphere counterpart to this rain axis existed in the pattern of heavy rain in the northeast corner of the Arabian Sea and north half of the Bay of Bengal.

Monthly rainfalls are summarized in time series of rainfall averaged over the Ocean (Figure 4.11). Overall, monthly rainfall was fairly steady, varying at most by 30% from the three-year mean. It tended to be lightest during February and March; heaviest during May and June. In two respects 1979 was anomalous. Compared to 1980 and 1981, variability was damped. Further, the dominant frequency in this variability was bimonthly rather than seasonal.

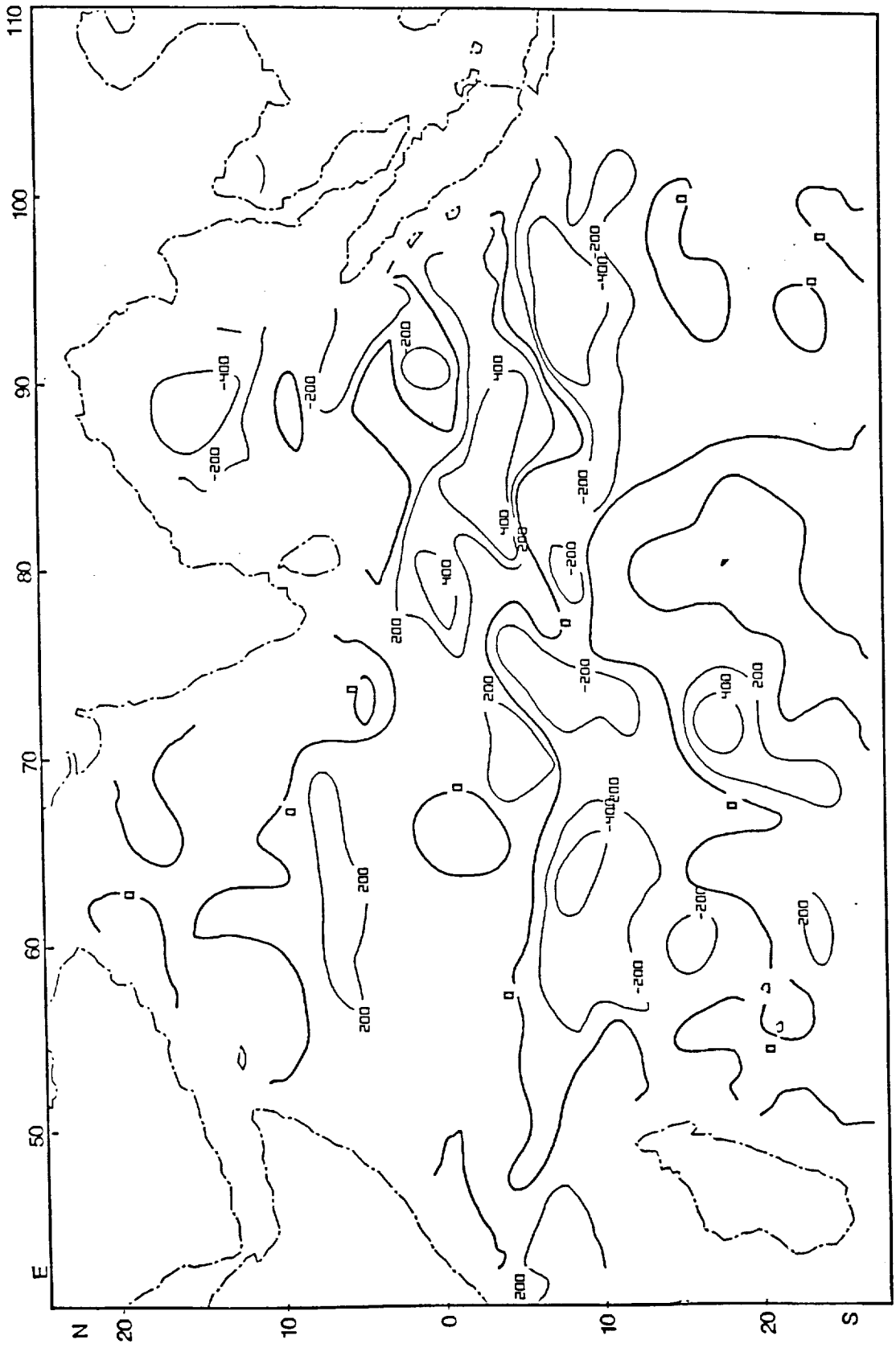

FIG. 4.9a 1979 departure of annual rainfall from the three-year mean. Positive values indicate annual rainfall greater than the mean. Units are millimeters.

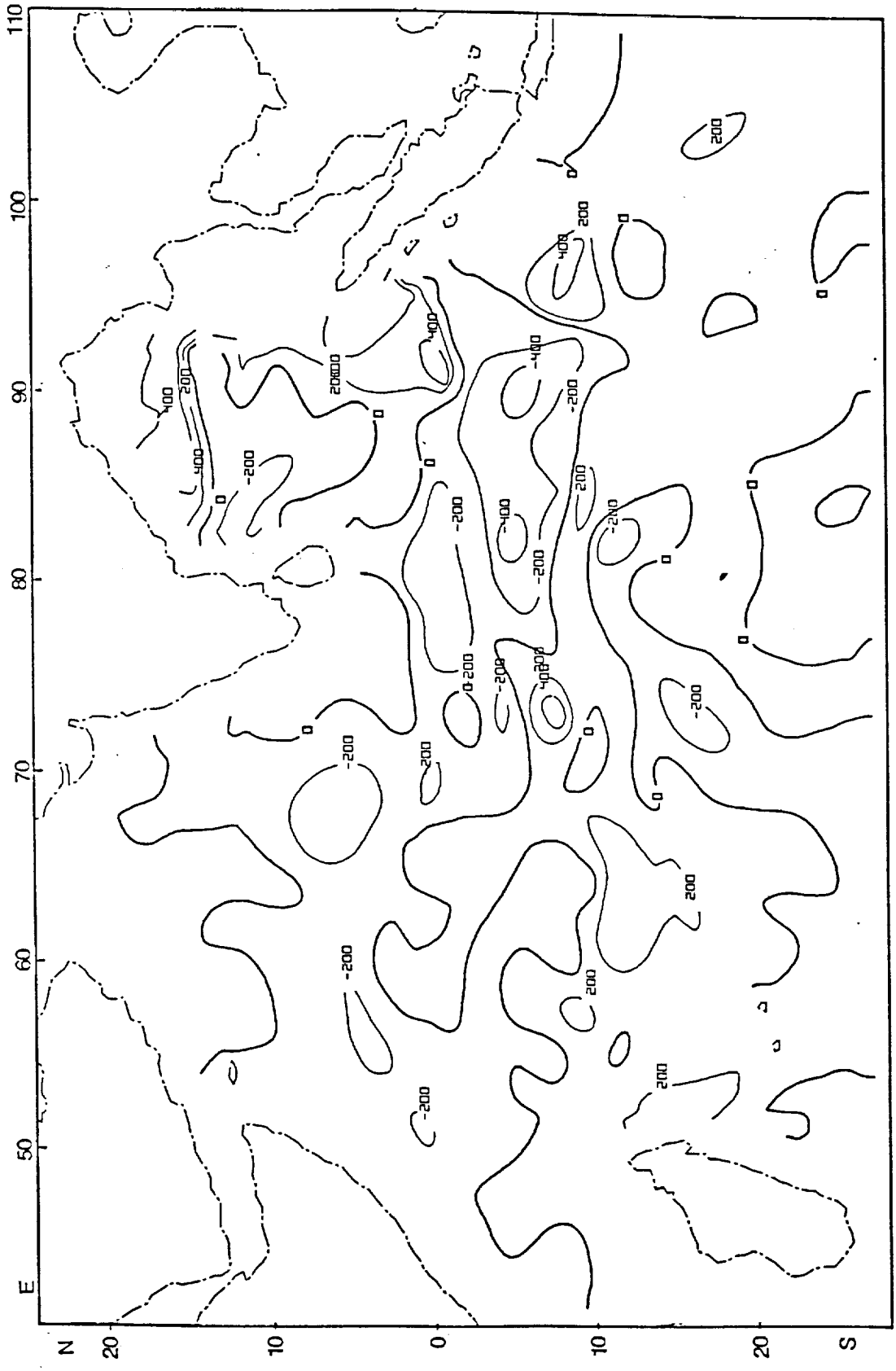

FIG. 4.9b Same as Figure 4.9a, except 1980.

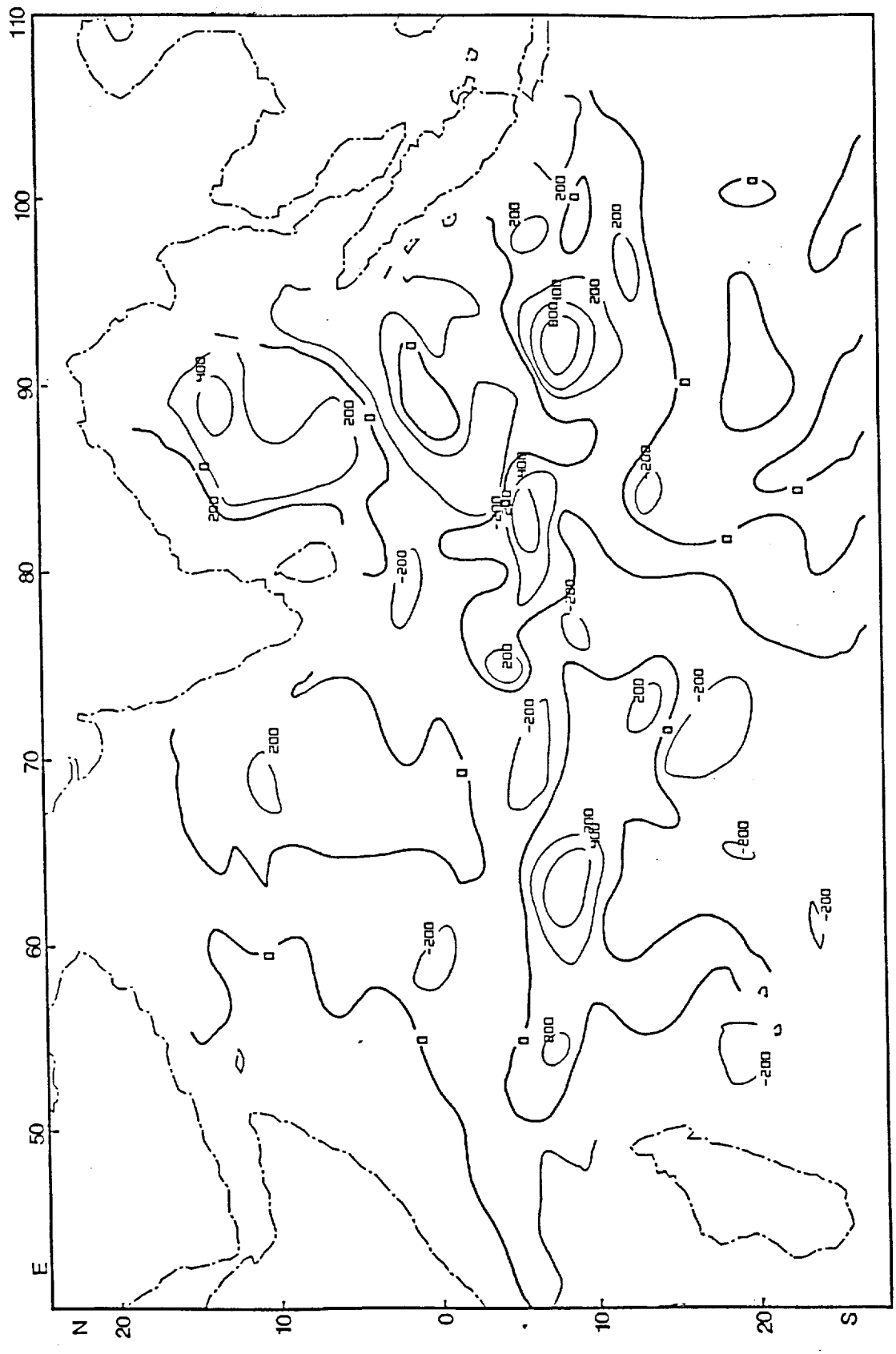

FIG. 4.9c Same as Figure 4.9a, except 1981.

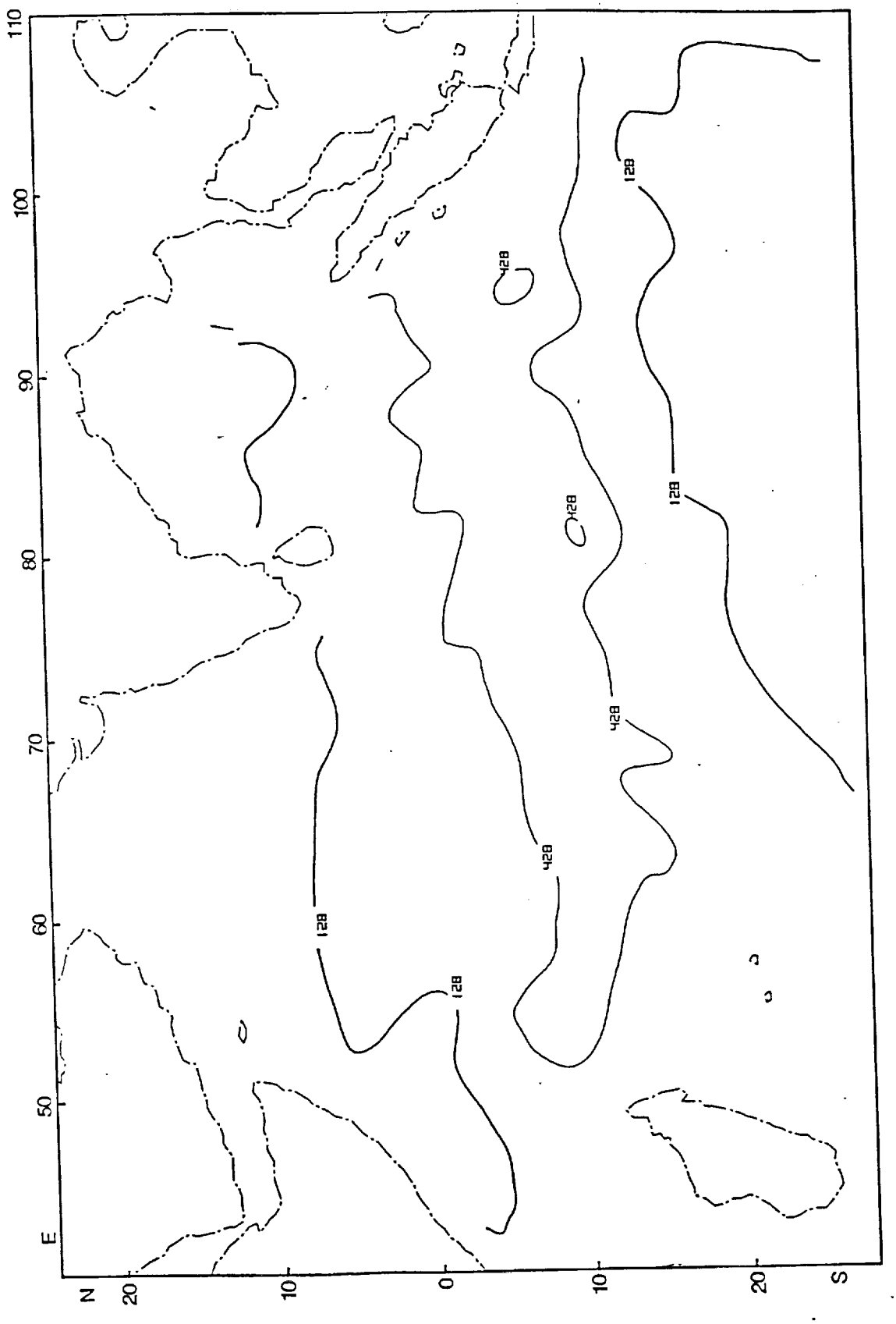

FIG. 4.10a Boreal winter seasonal accumulation of rainfall, in millimeters.

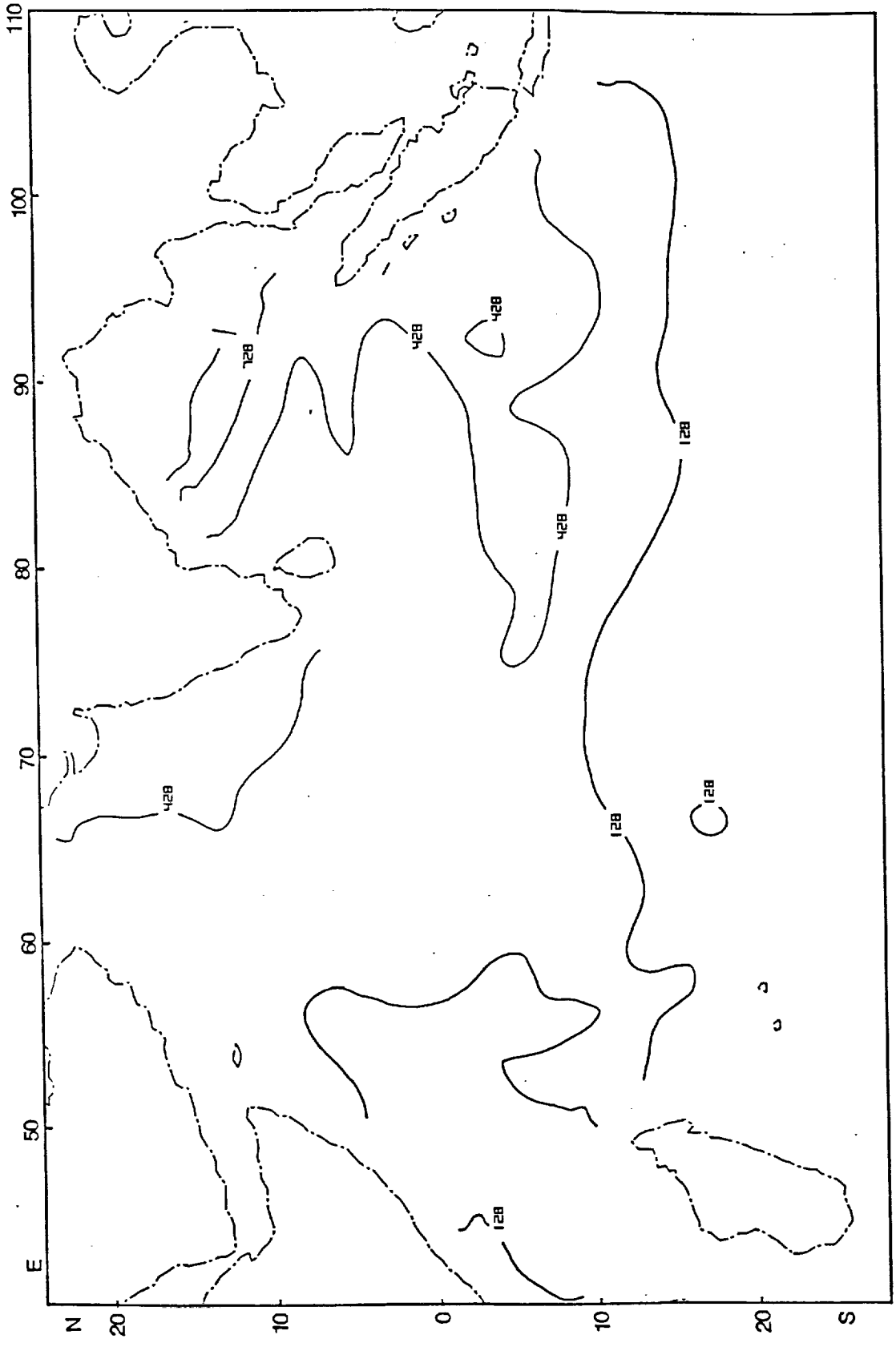

FIG. 4.10b Same as Figure 4.10a except, boreal summer.

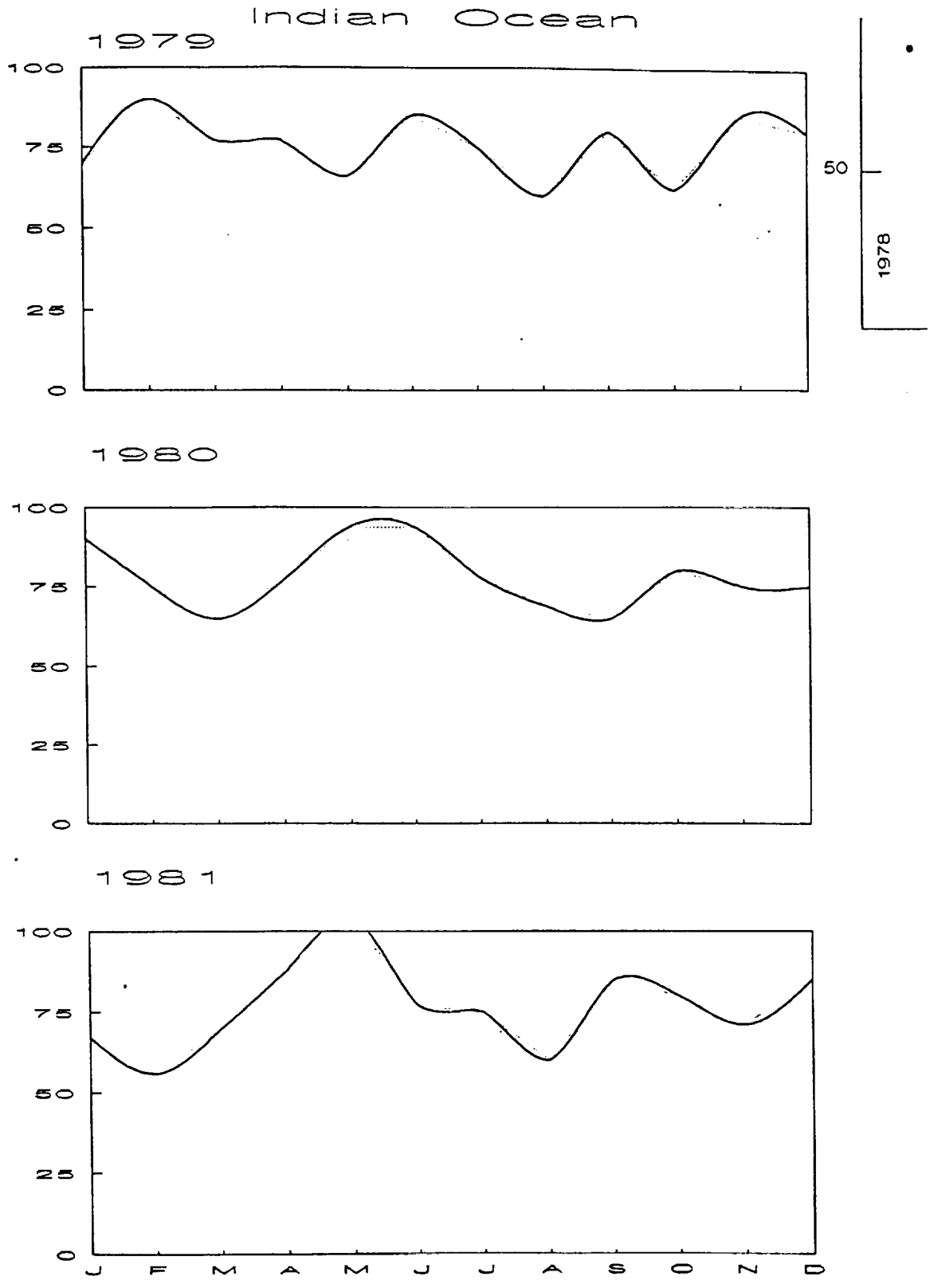

FIG. 4.11 Time series of rainfall averaged over the Indian Ocean. Units are millimeters.

Because of their proximity to Asia and influence on weather over India, the Arabian Sea and Bay of Bengal are places of special interest. As Table 4.5 shows, although in the mean the Bay was more than twice as wet, rainfall over the Arabian Sea was by no means negligible. In fact, if the Himalayan foothill districts are excluded, rainfall over the Arabian Sea amounted to 85% of the climatological mean annual rainfall over India.

Departures in the two basins tended to be out of phase. However, the amplitude of changes from year to year was small.

The annual curves of rainfall for the Arabian Sea are dominated by a single impulse which peaks in late May or June (Figure 4.12). Within the resolution of the analysis, this impulse coincides with the spike which Flohn (1960) observed for the central Arabian Sea in many years of ship reports of the occurrence of rain. In 1979, at least, it was linked to the onset of the summer monsoon (Krishnamurti, *et al.* 1981; Martin and Howland 1982, 1983). There is in addition a second impulse of much smaller amplitude. This follows the onset impulse by four to five months.

In curves of rain over the Bay of Bengal there also is an onset impulse and at least a hint of a secondary impulse (Figure 4.13). However, over the Bay the onset impulse starts earlier and tends to peak later. The secondary impulse is very broad. It maintains high rain rates into November.

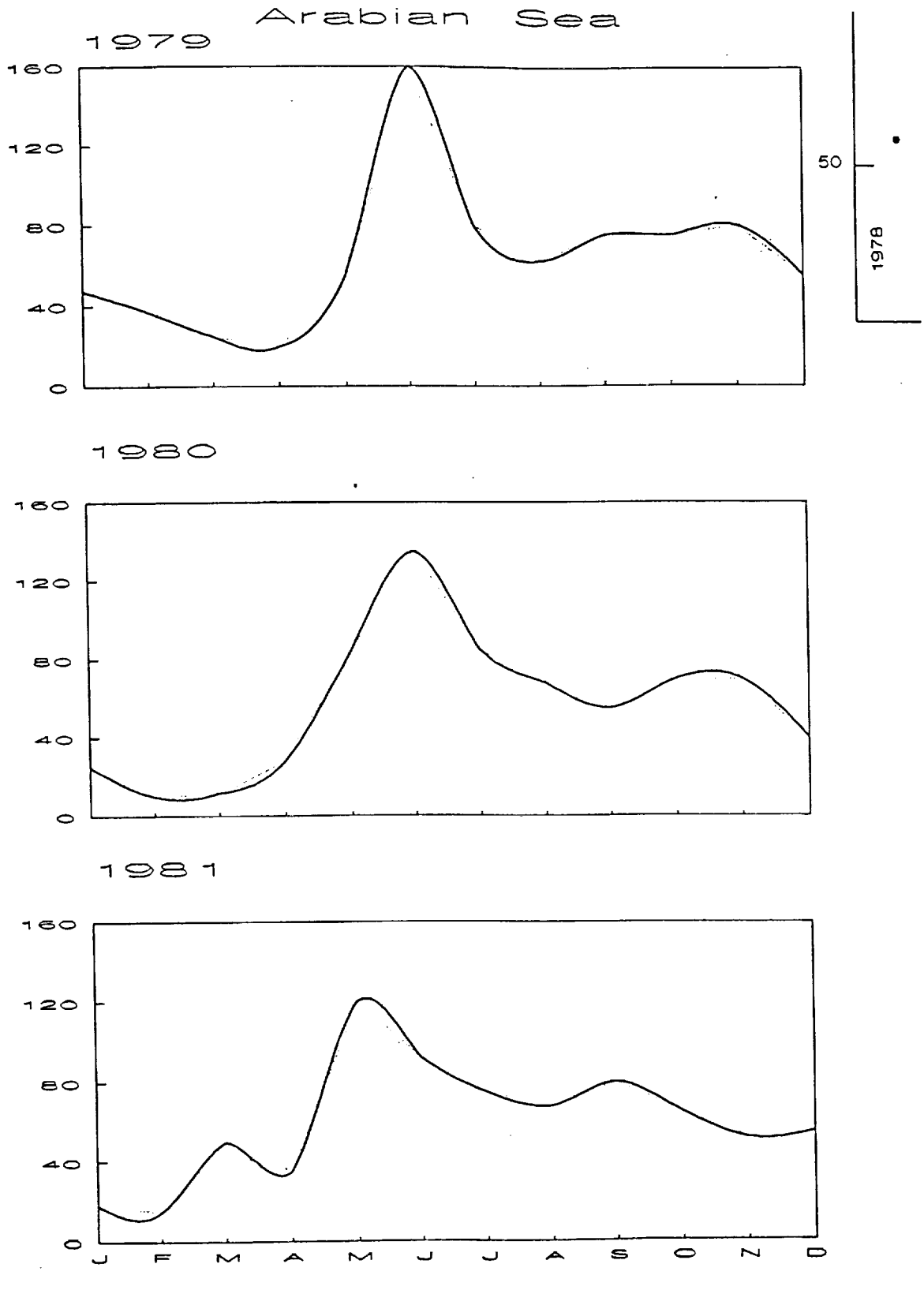

FIG. 4.12 Same as Figure 4.11, except Arabian Sea.

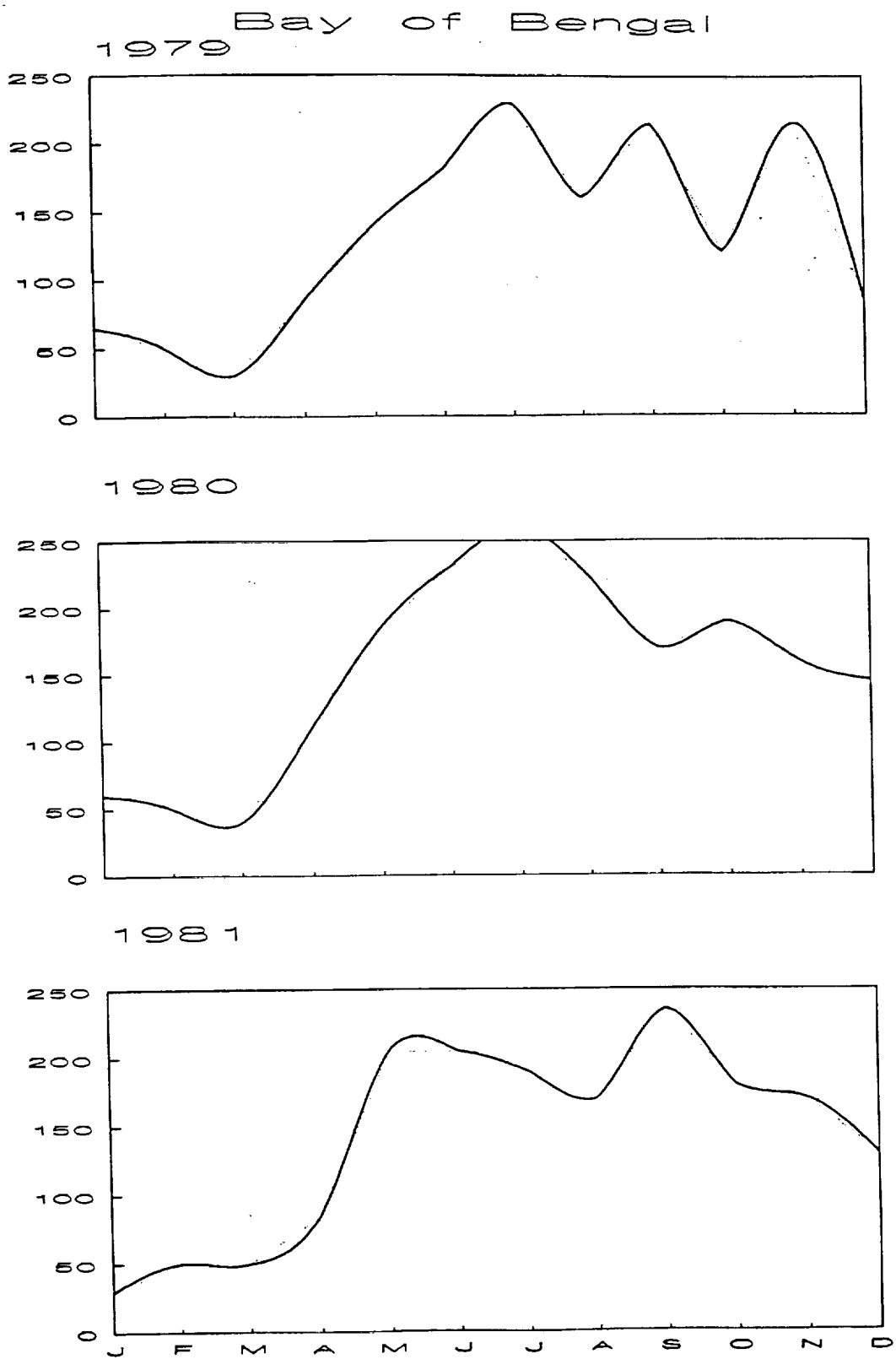

FIG. 4.13 Same as Figure 4.11, except Bay of Bengal.

5.0 CONCLUDING REMARKS

By exploiting observations of the Scanning Multi-channel Microwave Radiometer we have sought to attain a definitive mapping of Indian Ocean rainfall for the first three years in the life of Nimbus 7. The mapping employs a new algorithm which makes use of multiple frequencies in a statistical-physical model. The algorithm is fast, economical and superior to a single-channel algorithm. It appears to give meaningful results on scales as small as 200 km and a single month; however, owing to an uncertainty in cloud liquid water, in its present formulation the algorithm may underestimate Indian Ocean rainfall.

Applying this algorithm to SMMR data for the years 1979, 1980 and 1981, we find that Indian Ocean rainfall is less variable than sub-continental rainfall. Also, structure in rainfall along the coast of the sub-continent reflects structure in rainfall offshore. Finally, by almost any standard, Arabian Sea rainfall is significant. On balance we conclude that the statistical-physical model is a viable approach to retrieving rainfall over the Indian Ocean.

To resolve the question of bias, we recommend, first, that the cloud-liquid-water issue be resolved and, second, that the subdivision evaluation be extended to three whole years. To fill the gap in the 1979-1981 analysis, rainfall fields should be inspected for a signal in the 40-60 day period. Finally, to complete the SMMR Indian Ocean analysis and increase confidence in present results, the mapping should be extended through 1986.

6.0 ACKNOWLEDGEMENTS

For their assistance in reaching the goals of this study, we would like to give our special thanks to Phil Arkin, Per Gloersen, Raul Lopez, Jim Ridout, Peter Dodge, Frank Marks, David Santek and the McIDAS operations staff under Dee Wade.

7.0 REFERENCES

Ananthakrishnan, R., 1978: Some aspects of the monsoon circulation and monsoon rainfall. In *Monsoon Dynamics* (T.N. Krishnamurti, ed.), Birkhauser Verlag, Basel, 1209-1249.

Arkin, P.A., 1983: A diagnostic precipitation index from infrared satellite imagery. *Tropical Ocean. Atmos. Newsletter*, **17**, 5-7.

Battan, L. J., 1973: *Radar Observations of the Atmosphere.*, University of Chicago Press, Chicago.

Dorman, C.E., 1982: Indian Ocean rainfall. *Tropical Ocean-Atmosphere Newsletter*, **10**, 4

Flohn, H., 1960: Recent investigations on the mechanism of the "summer monsoon" of southern and eastern Asia. In *Monsoons of the World* (S. Basu *et al.*, eds.), pp. 75-88. Hind Union Press, New Delhi.

Geiger, R., 1965: *Jahrlicher Niederschlag.* Perthes Verlag, Darmstadt.

Gloerson, P., and L. Hardis, 1978: The scanning multichannel microwave radiometer (SMMR) experiment. In *The Nimbus-7 Users' Guide*, Goddard Space Flight Center, Greenbelt, MD, 213-245.

Hane, C. E., C. L. Ziegler, and P. S. Ray, 1982: Use of velocity fields from Doppler radars to retrieve other variables in thunderstorms. In *Instruments and Techniques for Thunderstorm Observation and Analysis*, Volume 3 of *Thunderstorms: A Social Scientific, and Technological Documentary*, (second edition) E. Kessler, (ed.), University of Oklahoma Press, Norman and London.

Hartmann, D.L. and M.L. Michelsen, 1989: Intraseasonal periodicities in Indian rainfall. *J. Atmos. Sci.*, **46**, 2838-2862.

Hastenrath, S., and P.J. Lamb, 1979: *Climatic Atlas of the Indian Ocean. Part I: Surface Climate and Atmospheric Circulation.* University of Wisconsin Press, Madison, 19pp.

Hinton, B.B., 1987: Rainfall over the tropical oceans during the special observing periods of the Global Weather Experiemnt, *Final Report on Grant NA85 AA-D-CA061*, Speace Science and Engineering Center, University of Wisconsin-Madison, Madison, 53706.

Hinton, B. B. and W. S. Olson, 1988: An approach to studies of interannual variations of rainfall using multifrequency dual polarization microwave radiances. In *Tropical Rainfall Measurements.*, Proceedings of the International Symposium on Tropical Precipitation Measurements, Tokai University, Tokyo, 28-30 October 1987, J. S. Theon and N. Fugono, eds., A. Deepak Publishing, Hampton, Va.

Jordan, C.L., 1958: Mean soundings for the West Indies area. *J. Meteor.*, **15**, 91-97.

Keenen, T.D., G.J. Holland, M.J. Manton and J. Simpson, 1988: TRMM ground truth in a monsoon environment: Darwin, Australia., *Austral. Meteor. Mag.*, **36**, 81-90.

Kilonsky, B.J., and C.S. Ramage, 1976: A technique for estimating tropical open-ocean rainfall from satellite observations. *J. Appl. Meteorol.* **15**, 972-5.

Krishnamurti, T.N., P. Ardanuy, Y. Ramanathan, and R. Pasch, 1981: On the onset vortex of the summer monsoon. *Mon. Wea Rev.* **109**, 344-363.

Kummerow, C., and J. A. Weinman, 1988: Determining microwave brightness temperatures from precipitating horizontally finite and vertically structured clouds., *J. Geophys. Res.*, **93**, 3720-3728.

Martin, D.W. and M.R. Howland, 1982: Rainfall over the Arabian Sea during the onset of the 1979 monsoon. *Nature*, **300**, 628-630.

Martin, D.W. and M.R. Howland, 1983: Daily Arabian Sea rainfall during the onset of the 1979 monsoon: A satellite estimate. *Papers in Meteor. Res.* (Taipei), 6, 91-100.

Mooley D.A. and J. Shukla, 1987: Variability and forecasting of the summer monsoon rainfall over India. *Monsoon Meteorology*, C.-P. Chang and T.N. Krishnamurti, eds., Oxford University Press, New York, 26-59.

Olson, W. S., 1989: Physical retrieval of rainfall rates over the ocean by multispectral microwave radiometry: Application to tropical cyclones., *J. Geophys. Res.*, **94**, 2267-2280.

Prabhakara, C., D.A. Short, W. Wiscombe, R.S. Fraser and B.E. Vollmer, 1986: Rainfall over oceans inferred from Nimbus 7 SMMR: Application to 1982-83 El Nino. *J. Clim. Appl. Meteor.*, **25**, 1464-1474.

Ramage, C.S., 1984: Climate of the Indian Ocean north of 35°S. In *Climates of the Oceans, World Survey of Clmiatology, Vol. 15* (H. Van Loon, ed.), Elsevier Science Publishing Co., 603-671.

Rao M.S.V., W.V. Abbott III and J.S. Theon, 1976: *Satellite-derived Global Oceanic Rainfall Atlas (1973 and 1974)*. **NASA SP-410**, Washington, D.C., 31 pp.

Rosenkranz, P. W., 1975: Shape of the 5 mm oxygen band in the atmosphere., IEEE Trans. on Antennas and Prop., AP-23, 498-506.

Saha, K., 1974: Some aspects of the Arabian Sea summer monsoon. *Preprints, International Tropical Meteorology Meeting (Nairobi, 31 Jan- 7 Feb)*, American Meteorology Society, Boston, 62-67.

Shea, D.J., 1986: Climatological Atlas: 1950-1979. Surface Air Temperature, Precipitation, Sea-Level Pressure, and Sea-Surface Temperature (45S-90N). *Technical Note NCAR/TN-269+STR*, Nat. Cen. Atmos. Res., Boulder, CO, 77pp.

Shukla, J., 1987: Interannual variability of monsoons. In *Monsoons* (J.S. Fein and P.L. Stephens, eds.), John Wiley and Sons, New York, pp.399-463.

Short, D. A., 1988: A statistical-physical interpretation of ESMR-5 brightness temperatures over the GATE area. In *Tropical Rainfall Measurements.*, Proceedings of the International Symposium on Tropical precipitation Measurements, Tokai University, Tokyo, 28-30 Octobere 1987, J. S. Theon and N. Fugono, eds., A. Deepak Publishing, Hampton, Va.

Short, D. A., and G. R. North, 1989: The beam filling error in ESMR-5 obvservations of GATE rainfall. Submitted to *J. Geophys. Res.*

Staelin, D. H., 1966: Measurements and interpretation fo the microwave spectrum of the terestrial atmosphere near 1-cm wavelength., *J. Geophys. Res.*, **71**, 2875-2881.

Weinman, J. A., and R. Davies, 1978: Thermal microwave radiances from horizontally finite clouds of hydrometeors. *J. Geophys. Res.*, **83**, 3099-3107.

Wilheit, T. T., 1979: A model for the microwave emissivity of the ocean's surface as a function of wind speed., *IEEE Trans. on Geoscience Electron.*, **GE-17**, 244-249.

Wu, R., and J. A. Weinman, 1984: Microwave radiances from precipitating clouds containing aspherical ice, combined phase, and liquid hydrometeors., *J. Geophys. Res.*, 89, 7170-7178.